



### 저작자표시-비영리-변경금지 2.0 대한민국

이용자는 아래의 조건을 따르는 경우에 한하여 자유롭게

- 이 저작물을 복제, 배포, 전송, 전시, 공연 및 방송할 수 있습니다.

다음과 같은 조건을 따라야 합니다:



저작자표시. 귀하는 원 저작자를 표시하여야 합니다.



비영리. 귀하는 이 저작물을 영리 목적으로 이용할 수 없습니다.



변경금지. 귀하는 이 저작물을 개작, 변형 또는 가공할 수 없습니다.

- 귀하는, 이 저작물의 재이용이나 배포의 경우, 이 저작물에 적용된 이용허락조건을 명확하게 나타내어야 합니다.
- 저작권자로부터 별도의 허가를 받으면 이러한 조건들은 적용되지 않습니다.

저작권법에 따른 이용자의 권리와 책임은 위의 내용에 의하여 영향을 받지 않습니다.

이것은 [이용허락규약\(Legal Code\)](#)을 이해하기 쉽게 요약한 것입니다.

[Disclaimer](#)



공학박사 학위논문

**Electrode Parameters on the Performance of  
Anion Exchange Membrane Fuel Cells with  
Platinum and Non-Precious Metal Catalysts**

백금 및 비귀금속 촉매를 이용한 음이온  
교환막 연료전지의 성능에 미치는  
전극 인자들

2018년 2월

서울대학교 대학원

화학생물공학부

김민정

# **Electrode Parameters on the Performance of Anion Exchange Membrane Fuel Cells with Platinum and Non-Precious Metal Catalysts**

지도교수 성 영 은

이 논문을 공학박사 학위논문으로 제출함

2018년 2월

서울대학교 대학원

화학생물공학부

김민정

김민정의 공학박사 학위논문을 인준함

2018년 2월

위원장 권택호 (인)

부위원장 성영은 (인)

위원 최장우 (인)

위원 박원철 (인)

위원 유성종 (인)

## **Abstract**

# **Electrode Parameters on the Performance of Anion Exchange Membrane Fuel Cells with Platinum and Non-Precious Metal Catalysts**

Min Jeong Kim

School of Chemical and Biological Engineering  
Seoul National University

Anion exchange membrane fuel cells (AEMFCs) are the most promising alternative fuel cells for replacing proton exchange membrane fuel cells (PEMFCs) with the development of anion exchange polymer membranes. The numerous advantages of AEMFCs over conventional PEMFCs include having excellent fuel flexibility due to low overpotential for hydrocarbon fuel oxidation, less crossover of anodic fuels to the opposite direction leading to higher fuel efficiency, and reduced corrosion problems. The biggest advantage of AEMFCs is that they use inexpensive oxygen reduction catalysts like non-precious metals catalysts (NPMCs) and carbon-based catalysts because of the significant decrease of its oxygen reduction overpotential in alkali environments. The high cost of platinum (Pt), which is the most prevalent oxygen reduction catalyst, is one of the barriers to

expanding the market of fuel cells. Because the cost of the catalyst layer accounts for nearly half of the total material costs of a fuel cell stack, many researchers have focused on developing NPMCs instead. However, many cathodes made of NPMCs exhibited lower performance than Pt/C in the single-cell system even if they showed comparable or superior oxygen reduction activities to commercial Pt/C catalysts in a half-cell tests with rotating disk electrodes. In order to bring out the intrinsic electrochemical activity of these catalysts in a single-cell, it is important to understand and optimize the parameters in the membrane electrode assembly (MEA), which is the key component in the single-cell system. When the application of catalysts is extended from the half-cell to the single-cell, the parameters that are important for high performance are changed. One of the main reasons for the different trends between the half-cell and the single-cell results is because each have a different electrolyte type. In the case the half-cell system, almost all the active sites participate in the electrochemical reaction due to the use of liquid electrolyte solution. However, in the case of a single-cell system, only catalyst active sites at the triple-phase boundary, where the catalyst, solid electrolyte and reactant meet, contribute to the performance. The properties of the solid electrolyte and its distribution state in the catalyst layer play a key role in determining the ionic conductivity and microstructure of the catalyst layer, and therefore affect the performance of the single-cell system. Particularly, the ratio of the catalyst layer thickness to the membrane thickness is higher in AEMFCs than that in PEMFCs, therefore the ionic conductivity and mass transport can account for a larger portion

of the performance. The other main reason of different trends is the management of the reactant and product. For the single-cell system, the supply of reactants and the removal of products are much more complicated than in the half-cell system. For AEMFCs in particular, water is a product at the anode side as a result of hydrogen oxidation reaction (HOR), but also a reactant for the oxidation reduction reaction (ORR) at the cathode side. Therefore, water management is a tricky task and very important especially in terms of ionic and concentration overpotential.

In the first chapter, after a brief introduction about polymer electrolyte membrane fuel cells and MEA, a detailed overview of AEMFCs follows.

In the second chapter, the studies on the important parameters in terms of MEA are discussed for AEMFCs using platinum catalyst cathode. The first study describes a simple method for enhancing the performance of alkaline anion exchange membrane fuel cells (AEMFCs) by reducing their ohmic overpotentials in the catalyst layer. Performance was increased due to the replacement of  $\text{Cl}^-$  by  $\text{OH}^-$ , which acts as a counter ion in the commercial ionomer and has greater ion conductivity than  $\text{Cl}^-$ . The resistance characteristics of MEAs were verified by analyzing impedance spectroscopy results. Enhancement of ionic conductivity in the catalyst layer was larger in AEMFC with NPMCs. In addition, performance improvement by facilitating the mass transfer and ionic conduction in the catalyst layer through control of catalyst ink solution is discussed. The value of the dielectric constant of the solvent used for the dispersion of catalyst influences the pore structure in the catalyst layer and the performance of AEMFCs. For better water

management, the effect of the presence of the mesoporous layer (MPL) and the degree of hydrophobicity of the gas diffusion layer (GDL) on the performance of AEMFCs was investigated.

In the last chapter, strategies for improving the performance of AEMFCs using NPMCs are discussed by engineering electrode structure. In the NPMCs system, particularly in the case of carbon based catalysts, since the density of the active sites is much lower than that of commercial Pt catalysts, a higher loading amount of catalysts is required, which results in an increase in mass and ohmic transport resistance. Two approaches were used to overcome these challenges. The first approach is applying a two-dimensional carbon sheet as the cathode catalyst to the AEMFCs to accomplish the high volumetric current density attributed to the thin carbon sheet structure, which can reduce the diffusion length in the catalyst layer. The second approach is introducing the macroporous structure in the catalyst layer to enhance performance by improving the mass transfer, especially water diffusion, which is a critical factor for ionic conduction in the catalyst layer and a reactant for ORR.

**Keywords:** Membrane-electrode assembly (MEA), Anion Exchange Membrane Fuel Cells (AEMFCs), Electrochemistry, Non-precious metals catalysts (NPMCs), Catalyst layer structure.

**Student Number:** 2013-30278

## Contents

<b>Abstract .....</b>	<b>i</b>
<b>List of Tables.....</b>	<b>viii</b>
<b>List of Figures.....</b>	<b>ix</b>
<b>Chapter 1 Introduction .....</b>	<b>1</b>
1.1 General Introduction of Fuel Cells.....	1
1.2 Components of Polymer Electrolyte Membrane Fuel Cells (PEMFCs) .....	5
1.3 Performance Loss of PEMFCs.....	8
1.4 General Introduction of Anion Exchange Membrane Fuel Cells (AEMFCs) .....	11
1.5 Current status and Challenges of AEMFCs .....	14
1.6 References.....	22
<b>Chapter 2 Engineering the MEA parameters for Improving the Performance of AEMFCs with Platinum Cathode Catalyst.....</b>	<b>29</b>

2.1	Introduction.....	29
2.2	Experimental.....	33
2.2.1	Materials Preparation .....	33
2.2.2	Characterizations and Electrochemical Test.....	34
2.3	Results and Discussion .....	36
2.3.1	Activation Method.....	36
2.3.2	Effect of Catalyst Ink Solvents .....	50
2.3.3	Effect of Gas Diffusion Layer properties .....	60
2.4	Conclusion .....	71
2.5	References.....	72

### **Chapter 3 Strategies for Improving the Performance of AEMFCs with Non Precious Metal Cathode Catalysts ..... 78**

3.1	Introduction.....	78
3.2	Experimental.....	82
3.2.1	Materials Preparation.....	82
3.2.2	Characterization and Electrochemical Test .....	83
3.3	Results and Disscusion .....	85
3.3.1	Applying Carbon Sheet Structure to Cathode Catalyst for High Volumetric Performance of AEMFC.....	85
3.3.2	Tailoring the Secondary Pore Structure in the Cathode	

Catalyst Layer for Improving the Mass Transfer .....	93
3.4    Conclusion .....	104
3.5    References.....	106
<b>국문 초록 .....</b>	<b>112</b>

## **List of Tables**

Table 2.1	Physical parameters of various dispersion solvents.....	52
Table 2.2	Operating parameters.....	61
Table 2.3	The physical properties of GDLs .....	64

## List of Figures

Figure 1.1	Projected greenhouse gases for different alternative vehicle scenarios.....	3
Figure 1.2	Schematic of single-cell components and structure .....	7
Figure 1.3	Illustration of characteristics of I-V curves for three main losses .....	10
Figure 1.4	Schematic of proton-exchange membrane fuel cells (PEMFCs) and anion exchange membrane fuel cells (AEMFCs) .....	12
Figure 1.5	Direction of water movement in AEMFC.....	15
Figure 1.6	Two hydroxide ion transport mechanisms. Hydroxide ion (a) transport through the water channel by forming and breaking of continuous H-bonds line in H-bonds network and (b) traversed across quaternary ammonium groups by following the rotation about C-CH <sub>2</sub> single bond.....	17
Figure 2.1	Number of publications and citations per year about AEMFCs .....	31
Figure 2.2	(a) Polarization (●) and power density (○) curves of Pt/C catalyst, (b) current density at 0.6 V and (c) maximum power density of single-cells with DI- and KOH-treated MEAs.....	37
Figure 2.3	Cross sectional FE-SEM images of (a) DI- and (b) KOH-treated MEAs.....	38
Figure 2.4	(a) EDX spectrum and (b) FT-IR spectrum of solidified ionomer after DI and KOH treatments. ....	41

Figure 2.5	Nyquist impedance plots of the DI- and KOH-treated MEAs for H <sub>2</sub> /O <sub>2</sub> operation at constant current of -2 A .....	42
Figure 2.6	Equivalent circuit for the impedance of the catalyst layer of fuel cell under (a) the faradaic condition and (b) non-faradaic condition.....	44
Figure 2.7	(a) Nyquist impedance plots, (b) real part and (c) imaginary part of complex capacitances as a function of log scale frequency of the DI- and KOH-treated MEAs for H <sub>2</sub> /N <sub>2</sub> operation at 0.45 V.....	48
Figure 2.8	(a) Polarization (●) and power density (○) curves and (b) FE-SEM cross sectional FE-SEM image of MEA with NPMC. ....	49
Figure 2.9	The size distribution of ionomer agglomerates dispersed in the (a) tert-butanol, (b) 2-propanol and (c) ethanol. Inset images are an optical micrograph of ionomer dispersion. (d) Average size of ionomer aggregates in accordance to solvents with different dielectric constants .....	53
Figure 2.10	SEM images of the catalyst layer structure fabricated with different catalyst dispersion solvent. (a) tert-butanol, (b) 2-propanol and (c) ethanol solvents.....	54
Figure 2.11	Polarization curves of AEMFCs using MEAs prepared with different catalyst dispersion solvents under the conditions of (a) H <sub>2</sub> /O <sub>2</sub> and (b) H <sub>2</sub> /Air. (c) Oxygen gain as a function of current density .....	55
Figure 2.12	Nyquist impedance plots of AEMFCs using MEAs prepared with	

different catalyst dispersion solvents for H <sub>2</sub> /O <sub>2</sub> operation at constant current of (a) -1 A, (b) -5A and (c) -10 A .....	58
Figure 2.13 Nyquist impedance plot of AEMFCs using MEAs prepared with different catalyst dispersion solvents for H <sub>2</sub> /N <sub>2</sub> operation at open-circuit voltage .....	59
Figure 2.14 The amount of water detected and calculated according to the HOR and ORR at each side of electrode at constant current -3A.....	62
Figure 2.15 Cross sectional FE-SEM images of four different type of GDLs; (a) CP, (b) CP H, (c) CPM L and (d) CPM H .....	66
Figure 2.16 (a) Polarization curves and (b) Nyquist plots of AEMFC using CPM L and CPM H as the anode GDLs and CPM L as the cathode GDLs. (Nyquist plot measured at -5 A) .....	67
Figure 2.17 Polarization curves of AEMFC using CP, CP H, CPM L and CPM H as the cathode GDLs and CPM H as the anode GDLs.....	70
Figure 3.1 Reported catalysts loading of NPMCs compared to Pt catalyst in the half-cell system in several papers.....	80
Figure 3.2 Schematic illustration of synthesis of CS-FeN-C .....	86
Figure 3.3 FE-SEM images of CS-FeN-C (a) before, (b) after removal of NaCl and (c) its enlarged image. (d) TEM image of CS-FeN-C.....	87
Figure 3.4 FE-SEM cross sectional images of MEA with (a) CS-FeN-C and (b) CB-FeN-C. (c) Polarization (○, △) and power density (●, ▲) curves of AEMFCs using CS- and CB-FeN-C (normalized by	

	volume of cathode catalyst layer)..	89
Figure 3.5	FE-SEM cross sectional images of MEA with (a) CS-FeN-C and (b) Pt/C 40 wt%.	91
Figure 3.6	(a) ORR polarization curves of CS-FeN-C and Pt/C. (b) Polarization ( $\circ$ , $\triangle$ ) and power density ( $\bullet$ , $\blacktriangle$ ) curves of CS-FeN-C and Pt/C normalized by volume of cathode catalyst layer.	92
Figure 3.7	FE-SEM images of (a) LP_FeN-C and (b) SP_FeN-N. Magnified (c) SEM and (d) TEM images.....	94
Figure 3.8	(a) ORR polarization curves of LP_FeN-C and SP_FeN-C. (b) Polarization ( $\circ$ , $\triangle$ ) and power density ( $\bullet$ , $\blacktriangle$ ) curves of LP_FeN-C and SP_FeN-C.....	95
Figure 3.9	FE-SEM cross sectional images of MEA with (a) LP_FeN-C and (b) SP_FeN-C cathodes.	97
Figure 3.10	(a) Pore size distribution of LP_FeN-C and SP_FeN-C cathodes. (b) Changes in average secondary pore size and oxygen utilization in LP_FeN-C and SP_FeN-C cathodes.....	98
Figure 3.11	Polarization ( $\circ$ , $\triangle$ ) and power density ( $\bullet$ , $\blacktriangle$ ) curves of AEMFCs with LP_FeN-C and Pt/C cathodes..	101
Figure 3.12	FE-SEM cross sectional images of MEA with (a) LP_FeN-C and (b) Pt/C cathodes.....	102
Figure 3.13	(a) Pore size distribution of LP_FeN-C and Pt/C cathodes. (b)	

Oxygen gain as a function of current density for AEMFCs with LP_FeN-C and Pt/C cathodes.....	103
---	-----

# **Chapter 1    Introduction**

## **1.1    General Introduction of Fuel Cells**

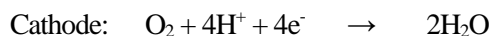
Fuel cells are an energy conversion device that change the chemical energy to electrical energy. Fuels (hydrogen, methanol and hydrazine etc.) react with oxidants (oxygen and air), concomitantly generating water and heat as byproducts and producing electricity as shown in the following equation.



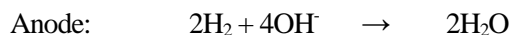
This reaction is spontaneous and thermodynamically favorable because the free energy of the water is less than that of hydrogen and oxygen. The theoretical standard potential of this reaction is 1.229 V at 298K.<sup>1-2</sup> The fuel cell was first called a gas voltaic battery when William Robert Grove invented it in 1842.<sup>3</sup> This earliest fuel cell consisted of two porous platinum foil electrodes, which are immersed in aqueous sulfuric acid purged with hydrogen and oxygen gas separately. This resulted in producing constant current. These electrochemical reactions were hydrogen oxidation reaction (HOR) and oxygen reduction reaction (ORR), which are termed as the half-cell reaction occurring at the anode and cathode, respectively. These half-cell reactions varied depending on the electrolyte type of fuel cell and changes in the charge carrier. The proton and hydroxide ions

are charge carriers in acidic and alkaline electrolytes, respectively, and the half-cell reactions take place at the anode and cathode as follows.

*In Acidic electrolytes,*



*In Alkaline electrolytes,*



Fuel cells are generally classified into six types, according to the electrolyte type; proton exchange membrane fuel cells (PEMFCs), direct methanol fuel cells (DMFCs), anion exchange membrane fuel cells (AEMFCs), phosphoric acid fuel cells (PAFCs), molten carbonate fuel cells (MCFCs), solid oxide fuel cells (SOFCs).

Among these, proton exchange membrane fuel cells (PEMFCs) have been the most intensively studied. They have been applied to fuel cell electric vehicles (FCEVs) as an alternative to the internal combustion engine. FCEVs have the potential to significantly reduce our dependence on foreign oil and lower harmful emissions that contribute to climate change. Computer simulations have been carried out to estimate the reduction effect of greenhouse gas emission. As shown in Figure 1.1, all types of electric vehicles reduce greenhouse gas emission, and

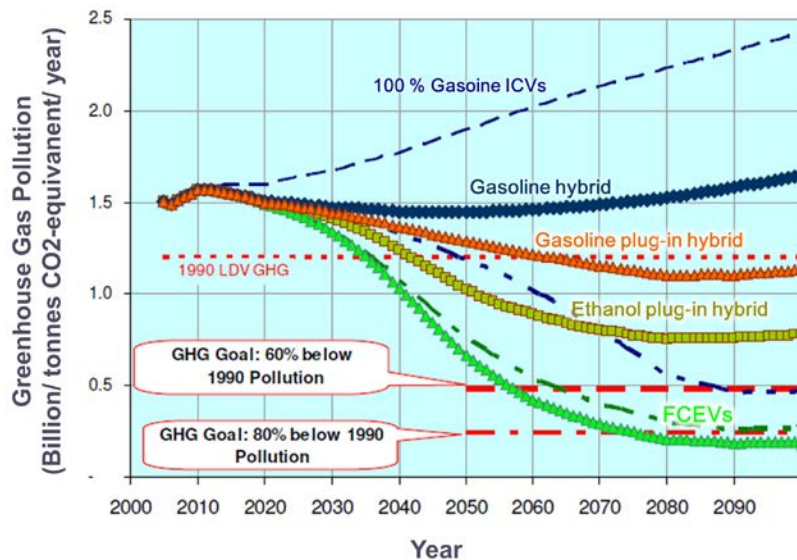


**Figure 1.1** Projected greenhouse gases for different alternative vehicle scenarios

[Sources: C.E. Thomas, the National Hydrogen Association Annual Meeting

documents]

the reduction rate of FCEVs is the largest among the electric vehicles studied.<sup>4</sup>

FCEVs produce their own electricity. Hydrogen fuel stored in the fuel tank is fed into a fuel cell stack. Then, air combines with the hydrogen fuel and a chemical reaction takes place generating electricity, which is directed to an electric motor. This fuel cell stack is composed of individual single-cells that are connected in a series to increase the voltage of the system.

## **1.2 Components of Polymer Electrolyte Membrane Fuel Cells (PEMFCs)**

This single-cell is composed of the bipolar plate, gas diffusion layers, catalyst layers for each side of electrode, and the polymer electrolyte membrane. The membrane-electrode-assembly (MEA), which is composed of gas diffusion layers, catalyst layers and the polymer electrolyte membrane, is the key component of single-cell and determine the performance of single-cell (Figure 1.2).

- (1) The catalyst layer is where the electrochemical reaction occurs and is deposited on each side of the membrane. A hydrogen electro-oxidation reaction and oxidation electro-reduction reaction occur at the anode and cathode side, respectively. The catalyst layer must have high electrochemical stability in the reaction environment of both electrodes.
- (2) The polymer electrolyte membrane acts not only as a conducting medium that permits counter ion to pass between the anode and cathode (proton for PEMFCs, hydroxide ion for AEMFCs), but it also as a separator that prevents physical contact between the two reaction gases. Therefore, the membrane should have a high counter ion conductivity but an electron conductivity close to zero. It should also have a low gas permeability to prevent the mixed potential due to the crossover phenomenon.

(3) The gas diffusion layers located between the catalyst layer and bipolar plate facilitate transport of the reactant to catalyst layer and removal of product from it. Therefore, high permeability to the reaction gas is required. In addition, it is necessary to sufficiently maintain the wetting of the electrolyte membrane, while allows generated water to be discharged without being flooded into the catalyst layer.

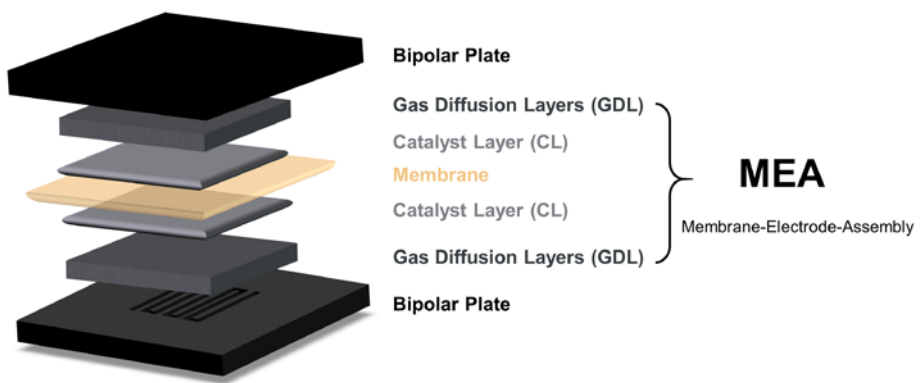


**Figure 1.2** Schematic of single-cell components and structure

### **1.3 Performance Loss of PEMFCs**

An ideal fuel cell maintains a constant voltage determined by thermodynamics, and supplies all the currents as long as sufficient fuel is supplied. The reversible open cell voltage of a fuel cell is related to the change in Gibbs free energy of the reaction as indicated by following equation.

$$E^0 = -\Delta G^0 / n \cdot F$$

The value of  $\Delta G^0$  is -237.13 kJ /mol when the produced water is liquid phase, n is 2, and hence the calculated value of  $E^0$  is 1.229 V.<sup>5</sup> However, the practical fuel cell voltage is less than the thermodynamically calculated voltage due to irreversible losses. There are three main types of losses in fuel cells, which are related to one of the steps in the fuel cell reaction. Their respective proportions depend on the current density, therefore, there is a characteristic current-voltage curve shape depending on the loss factor. (Figure 1.3). The types of losses are as follows.

- (1) Activation loss due to the reaction kinetics, which involves the transfer of electrons between an electrode surface and a reactant. This term is related to the intrinsic catalytic activity. Also, an increase in catalyst loading or active site density can reduce activation loss.
- (2) Ohmic loss from ionic and electronic resistance in the electrode, polymer electrolyte and interconnection. Therefore, it is possible to reduce the ohmic

loss by using a material (catalysts and supporting materials) that has high electron conductivity or an ionomer that has good ion conductivity. Since the ionic conductivity depends on the hydration state of the ionomer, the humidity control in the MEA is also important in reducing the ohmic loss.<sup>6</sup>

(3) Concentration loss due to mass transport that controls the supply and removal of reactants and products in fuel cells. The most well-known method to improve concentration loss is to control the pore structure of the catalyst layer. The pore structure in the catalyst layer is divided into two types in terms of MEA; the primary pore and the secondary pore. The primary pores exist inside and between the primary particles in the agglomerate. It acts as a reaction sites in the range of mesopores (smaller than 50 nm). The secondary pores are present between the aggregates in a range greater than 50 nm. These are the transport pathway of reactants and products in the catalyst layer.<sup>7</sup>

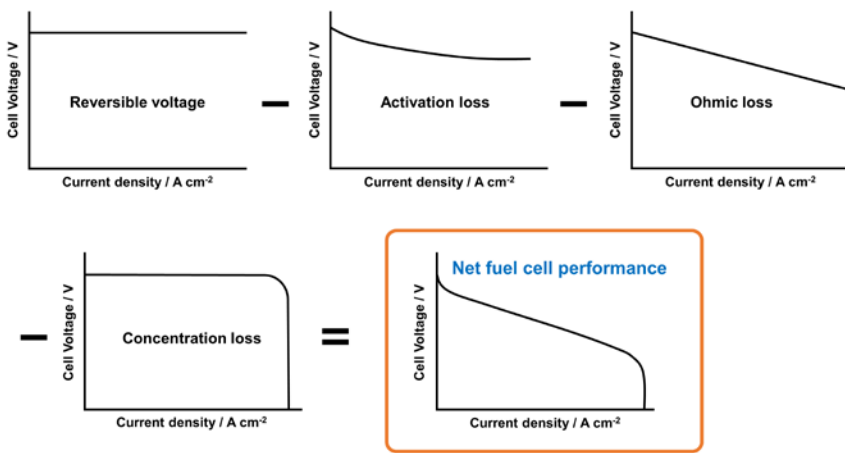
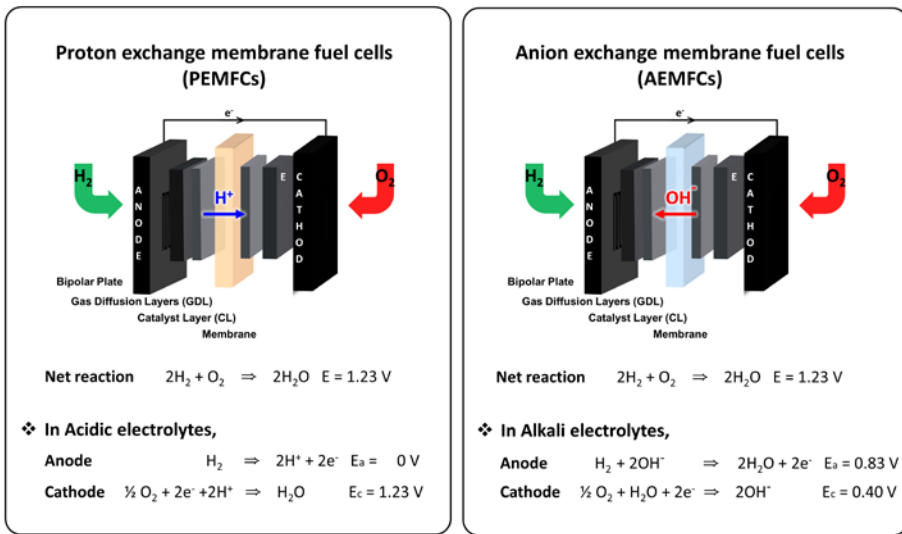


Figure 1.3 Illustration of characteristics of I-V curves for three main losses<sup>5</sup>

## **1.4 General Introduction of Anion Exchange Membrane Fuel Cells (AEMFCs)**

The alkaline fuel cell was the first type of fuel cell widely used in an industrial application in 1960s for the U.S space program to produce electrical energy and water onboard their spacecraft.<sup>8</sup> Early alkaline fuel cells used a liquid electrolyte solution, in which potassium hydroxide was dissolved in water. However, because of this structure, it has suffered from problems like liquid electrolytes leaking and carbonate precipitation caused by reactions with CO<sub>2</sub>. These difficulties lead to the prohibition of widespread usage of alkaline fuel cells (AFCs) as an alternative energy source. Since the development of an anion exchange membrane that was able to conduct hydroxide ion, there has been increasing interest worldwide for developing AFCs which use a polymer membrane instead of liquid electrolytes. AFCs using polymer membrane are generally called anion exchange membrane fuel cells (AEMFCs), alkaline membrane fuel cells (AMFCs) or hydroxide exchange membrane fuel cells (HEMFCs). AEMFCs are very similar in structure to PEMFCs but the reaction mechanism and main issues are very different (Figure 1.4).

The advantages of AEMFCs over conventional PEMFCs are summarized as follows. (1) The electrode kinetics of the cathode reduction reaction are much more facile in a high-pH (alkaline) environment compared to the lower-pH (acidic) environment in PEMFCs<sup>9,10</sup>; (2) various Pt-free materials like Co, Cu, Ag, Ni,



**Figure 1.4** Schematic of proton-exchange membrane fuel cells (PEMFC) and anion exchange membrane fuel cells (AEMFCs).

N-doped carbon, and perovskite can be used as catalysts in AEMFCs, whereas almost every catalyst containing non-noble metals are unstable in the acidic environment of PEMFCs<sup>11-15</sup>; (3) fuel flexibility is excellent due to the low overpotential of hydrocarbon fuel oxidation<sup>16-19</sup>; and (4) the crossover of anodic fuels to the opposite direction are suppressed because hydroxide anion and electro-osmotically driven water molecules generally migrate from cathode to anode.

## **1.5 Current status and Challenges of AEMFCs**

Early studies on AEMFCs focused on improving the hydroxide conductivity in anion exchange membrane (AEM) because the activation energy for the hydroxide conduction in AEM was nearly two times that of the proton conduction in proton exchange membrane (e.g. Nafion).<sup>20</sup> As a result of intensive research to develop AEM since early 2000, the hydroxide conductivity has increased from about 20 mS cm<sup>-1</sup> to 130 mS cm<sup>-1</sup> and the maximum power density of AEMFCs is 1160 mW cm<sup>-2</sup>, comparable to that of PEMFCs. However, there are still several challenges to be solved for commercialization.<sup>21</sup>

One of the significant challenges is water management under the operando conditions. Water management in AEMFCs plays an important role in determining the performance of fuel cells but it is also more complicated than in PEMFCs. This is because water is a product of the hydrogen oxidation reaction and simultaneously a reactant for oxygen reduction reaction during cell operation. Therefore, water flooding should be prevented at the anode side and water should not dry out at the cathode side. Research on the water management in the device has been carried out in recent years.<sup>22-25</sup> In AEMFCs, water is moved from the cathode to the anode by electro-osmotic drag and also can be opposite from the anode to the cathode by back diffusion due to the water concentration gradient (Figure 1.5). The dominant direction and the amount of water transport is

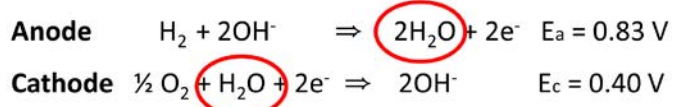
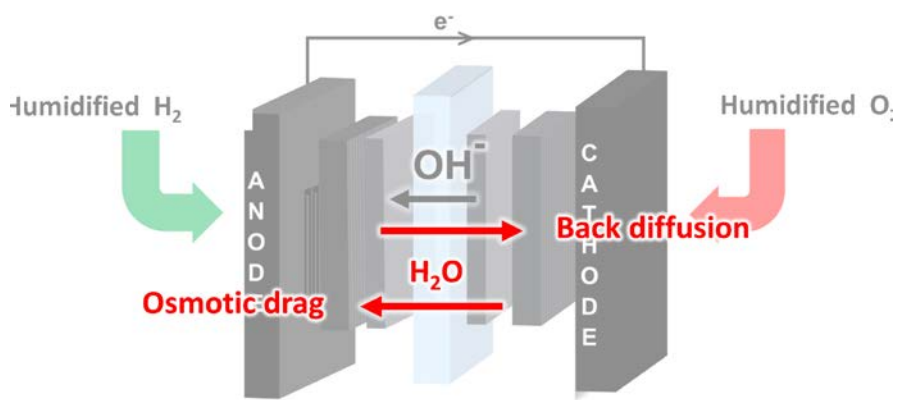
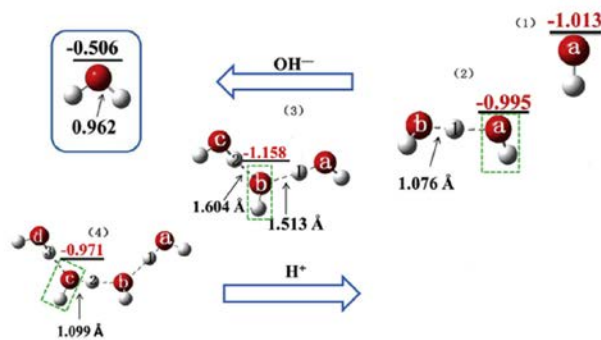


**Figure 1.5** Direction of water movement in AEMFC.

determined by the properties of AEM. Han Zhang et al.<sup>26</sup> insist that the cell performance can be improved by promoting the back diffusion using the hydrophilic AEM and controlling the relative humidity of anode gas to prevent the water flooding. Also, hydration state in the AEMFCs also impact on the activation energy for the hydroxide conduction in AEM. The hydroxide ion transport mechanisms are considered to be Grotthuss and Vehicular mechanisms based on the research using the molecular dynamics and density functional theory (DFT). Guoqing Yang et al. demonstrated two minimum energy pathways for hydroxide transport (Figure 1.6) in AEM and used DFT to calculate the energy barrier in the rate determining step, which is significantly reduced in water solutions.<sup>27</sup>

Low long-term stability is one of the factors preventing commercialization of AEMFCs. There are two main reasons that inhibits the stability of the membrane. One is the nucleophilic attack that occurs when the hydroxide transport from the cathode to anode. The nucleophilic OH<sup>-</sup> anions can react with the functional group in the ionomer and remove it, increasing ohmic resistance, in turn dramatically reducing the performance. Recently, it has been reported that the stability of the functional group can be improved by increasing the hydration number in the device.<sup>28</sup> Based on the DFT calculation and experiment, it was confirmed that as the number of water molecules solvating the hydroxide ion increases, the activation energy required for nucleophilic attack increases. The functional group was rapidly decomposed when

(a)



(b)

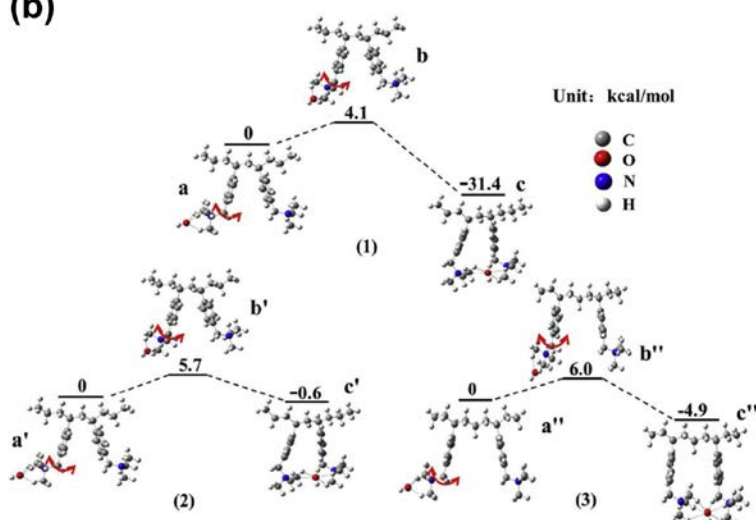


**Figure 1.6** Two hydroxide ion transport mechanisms. Hydroxide ion (a) transport through the water channel by forming and breaking of continuous H-bonds line in H-bonds network and (b) traversed across quaternary ammonium groups by following the rotation about  $\text{C}-\text{CH}_2$  single bond. (Adapted from Guoqing Yang et al. nt. J. Hydrot. Energy., 41, 6877-6884, 2016)

the hydration number was less than 4. Therefore, these results imply that maintaining a high hydration number in the actual device is crucial for ensuring the long-term stability of AEM and AEI.

The other reason for the stability issue of AEMFCs is its susceptibility to poisoning by carbon dioxide ( $\text{CO}_2$ ). It has been demonstrated in many papers that performance of AEM are still considerably affected by  $\text{CO}_2$ .<sup>29-31</sup> Although precipitation of metal hydroxide cannot occur because cationic moieties are fixed to the polymer chain and are not freely mobile as in a liquid electrolyte, hydroxyl ion is substituted to  $\text{CO}_3^{2-}$  or  $\text{HCO}^{3-}$  when exposed to air (see reaction (1) and (2))<sup>29</sup>



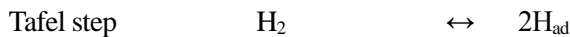
Carbonation of hydroxide ions increases the ohmic resistance and lowers the local pH at the anode side, thereby degrading the performance of the AEMFCs. Yanagi et al.<sup>32</sup> reported rapid exchange of  $\text{OH}^-$  in AEM to carbonate form within 30 min after it was exposed to air, leading to a decrease in ionic conductivity of AEM by a factor of about 1/4 (42 mS cm<sup>-1</sup> to 10 mS cm<sup>-1</sup>). More importantly, Gunasekara et al.<sup>33</sup> has reported on the effect of carbonate exchange on the half-cell performance with the membrane while introducing humid gas. As a result, it seems not to change the ORR kinetics that much, but lowering the oxygen

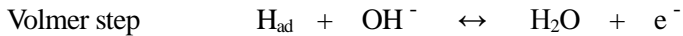
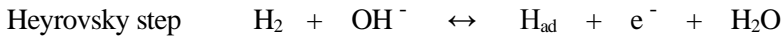
permeability by one order of magnitude hindering the mass transport of the reactant. Bharath et al.<sup>34</sup> reported the correlation between this CO<sub>2</sub> uptake and the degree of membrane hydration; the increase in hydration level opens the pores of the membrane, increasing the approach of CO<sub>2</sub> and thus increasing the interaction between cationic head groups and carbonate ions. Varcoe et al.<sup>35</sup> proposed the self-purging method in which the carbonate ions are released from the anode as CO<sub>2</sub> and replaced with OH<sup>-</sup> by activating the AEMFCs at a high current density as shown in the following equation.<sup>20,35</sup>



Recently, Katayama et al.<sup>36</sup> reported on the new approach to improve the CO<sub>2</sub> tolerance. Under the supply of H<sub>2</sub> gas containing NH<sub>3</sub> to anode and ambient air to the cathode, the performance of the AEMFC was improved compared to the performance of the AEMFC with supply of pure hydrogen to anode.

Low HOR performance in AEMFCs is another critical issue. In an alkaline environment, HOR proceeds to either Tafel–Volmer or Heyrovsky–Volmer reactions as shown in the following reaction equations.<sup>37</sup>





HOR kinetics on Pt are several orders of magnitude slower in alkaline electrolytes than in acidic electrolytes.<sup>8</sup> Therefore, it is crucial to establish the reason for poor HOR activity in alkaline electrolytes and develop the high performance of HOR catalysts.

It has been known that the use of PtRu as the anode catalyst exhibits higher performance in a single-cell as well as a half cell in an alkaline electrolyte than when Pt is used as an anode catalyst.<sup>38, 39</sup> However, the reason for the performance improvement of PtRu is under debate. The first interpretation of the reason for improvement is the bifunctional effect proposed by Strmcnik et al.<sup>39</sup> Ru, which has stronger oxophilicity than Pt, provides active sites for the adsorption of hydroxides and reacts with hydrogen absorbed on the Pt surface, promoting the HOR reaction. The enhancement of HOR performance as an anode catalyst of Pd-CeO<sub>2</sub> was also interpreted as a bifunctional effect.<sup>40</sup> The other interpretation is the electronic effect. The alloy of Pt and Ru accelerates the HOR by changing the electronic structure of Pt and lowering the binding energy of the hydrogen adsorbed on the Pt surface.<sup>38,41</sup> Besides the low intrinsic catalytic activity of Pt in alkaline conditions, another reason for low HOR performance is

due to the interaction between the functional groups of ionomer and Pt surface.

Chunk et al.<sup>42</sup> reported that the cationic functional group-hydroxide-water adsorption layer on the Pt surface inhibits hydrogen diffusion, resulting in low HOR activity.

## 1.6 References

1. O. Pilatowsky, R. J. Romeo, C. A. Isaza, S. A. Gamboa, P. J. Sebastian, W. Rivera, *Cogeneration fuel cell-sorption air conditioning systems*, Springer Science & Business Media, 2011.
2. J. Larminie, A. Dicks, *Fuel cell systems explained*, SAE International and John Wiley & Sons, 2003.
3. J. Wisniak, *Electrochemistry and Fuel Cells: The Contribution of William Robert Grove*, Indian Journal of History of Science, 50.3, 476-490, 2015.
4. The National Hydrogen Association, *Comparison of plug-in hybrids, fuel cell EVs and battery EVs*, [http://www.hydrogen.energy.gov/pdfs/htac\\_july09\\_10\\_h2gen.pdf](http://www.hydrogen.energy.gov/pdfs/htac_july09_10_h2gen.pdf)
5. R. O'Hayre, S. Cha, W. Colella, F. B. Prinz, *Fuel cell fundamentals*, John Wiley & Sons, 2009.
6. S Balog, U Gasser, K Mortensen, K. Mortensen, L. Gubler, G G Scherer, H. B. youcef, *Correlation between Morphology, Water Uptake, and Proton Conductivity in Radiation-Grafted Proton-Exchange Membranes*, Macromolecular Chemistry and Physics, 211, 635-643, 2010.
7. M Uchida, Y Fukuoka, Y Sugawara, N Eda, A. Ohta, *Effects of Microstructure of*

*Carbon Support in the Catalyst Layer on the Performance of Polymer-Electrolyte Fuel Cells*, Journal of the Electrochemical Society, 143, 2245-2252, 1996.

8. M. Warshay, P. R. Prokopius, *The fuel cell in space: yesterday, today and tomorrow*, Journal of Power Sources, 29, 193-200, 1990.
9. B.B. Blizanac, P.N. Ross, N.M. Markovic, *Oxygen electroreduction on Ag(1 1 1): The pH effect*, Electrochimica Acta, 52, 2264–2271, 2007.
10. W. Sheng, H. A. Gasteiger, Y. Shao-Horn, *Hydrogen oxidation and evolution reaction kinetics on platinum: acid vs alkaline electrolytes*, Journal of the Electrochemical Society, 157, B1529-B1536, 2010.
11. Q. Hu, G Li, J. Pan, L. Tan, J. Lu, L. Zhuang, *Alkaline polymer electrolyte fuel cell with Ni-based anode and Co-based cathode*, International Journal of Hydrogen Energy, 38, 16264–16268, 2013.
12. K. Miyazaki, N. Sugimura, K. Matsuoka, Y. Iriyama, T. Abea, M. Matsuoka, Z. Ogumia, *Perovskite-type oxides  $La_{1-x}Sr_xMnO_3$  for cathode catalysts in direct ethylene glycol alkaline fuel cells*, Journal of Power Sources 178, 683–686, 2008.
13. A. Kucernak, F. Bidault, G. Smith, *Membrane electrode assemblies based on porous silver electrodes for alkaline anion exchange membrane fuel cells*, Electrochimica Acta, 82, 284– 290, 2012.

14. C. Coutanceau, L. Demarconnay, C. Lamy, J.-M. Léger, *Development of electrocatalysts for solid alkaline fuel cell (SAFC)*, Journal of Power Sources, 156, 14–19, 2006.
15. T. Sakamoto, K. Asazawa, J. Sanabria-Chinchilla, U. Martinez, B. Halevi, P. Atanassov, P. Strasser, H. Tanaka, *Combinatorial discovery of Ni-based binary and ternary catalysts for hydrazine electrooxidation for use in anion exchange membrane fuel cells*, Journal of Power Sources, 247, 605–611, 2014.
16. C. Wang, B. Shen, C. Xu, X. Zhao, J. Li, *Side-chain-type poly (arylene ether sulfone)s containing multiple quaternary ammonium groups as anion exchange membranes*, Journal of Membrane Science, 492, 281–288, 2015.
17. N. Fujiwara, Z. Siroma, S. Yamazaki, T. Ioroi, H. Senoh, K. Yasuda, *Direct ethanol fuel cells using an anion exchange membrane*, Journal of Power Sources, 185, 621–626, 2008.
18. E. Antolinia, E.R. Gonzalez, *Alkaline direct alcohol fuel cells*, Journal of Power Sources, 195, 3431–3450, 2010.
19. K. Matsuoka, Y. Iriyama, T. Abe, M. Matsuoka, Z. Ogumia, *Alkaline direct alcohol fuel cells using an anion exchange membrane*, Journal of Power Sources, 150, 27–31, 2005.
20. S. Gottesfeld, D. R. Dekel, M. Page, C. Bae, Y. Yan, P. Zelenay, Y. S. Kim, *Anion*

- exchange membrane fuel cells: Current status and remaining challenges*, Journal of Power Sources, 375, 170-184, 2018.
21. L. Wang, E. Magliocca, E.L. Cunningham, W.E. Mustain, S.D. Poynton, R. Escudero-Cid, M.M. Nasef, J. Ponce-González, R. Bance-Souahli, R.C.T. Slade, D.K. Whelligan, J.R. Varcoea, *An optimised synthesis of high performance radiation-grafted anion-exchange membranes*, Green Chemistry, 19 , 831–843, 2017.
22. B. S. Machado, N. Chakraborty, P. K. Das, *Influences of flow direction, temperature and relative humidity on the performance of a representative anion exchange membrane fuel cell: A computational analysis*, International Journal of Hydrogen Energy, 42, 6310-6323, 2017.
23. S. Huo, H. Deng, Y. Chang, K. Jiao, *Water management in alkaline anion exchange membrane fuel cell anode*, International Journal of Hydrogen Energy, 37, 18389-18402, 2012.
24. H.-S. Shiau, I. V. Zenyuk, A. Z. Weber, *Water management in an alkaline-exchange-membrane fuel cell*, ECS Transactions, 69, 985-994, 2015.
25. Y.-J. Sohn, J. -I. Choi, K. Kim, *Numerical analysis on water transport in alkaline anion exchange membrane fuel cells*, Electrochemistry, 83, 80-83, 2015.
26. H. Zhang, H. Ohashi, T. Tamaki, T. Yamaguchi, *Water movement in a solid-state*

- alkaline fuel cell affected by the anion-exchange pore-filling membrane properties*, The Journal of Physical Chemistry C, 117, 16791-16801, 2013.
27. G Yang, J. Hao, J. Cheng, N. Zhang, G He, *Hydroxide ion transfer in anion exchange membrane: A density functional theory study*, International Journal of Hydrogen Energy, 41, 6877-6884, 2016.
28. D. R. Dekel, M. Amar, S.Willdorf, M. Kosa, S. Dhara, C. E. Diesendruck, *Effect of water on the stability of quaternary ammonium groups for anion exchange membrane fuel cell applications*, Chemistry of Materials, 29, 4425-4431, 2017.
29. T. D. Myles, K. N. Grew, A. A. Peracchio, W. K. S Chiu, *Transient ion exchange of anion exchange membranes exposed to carbon dioxide*, Journal of Power Sources, 296, 225-236, 2015.
30. J. A. Wrubel, A. A. Peracchio, B. N. Cassenti, T. D.Myles, K. N. Grew, W. K. S.Chiu, *Anion exchange membrane ionic conductivity in the presence of carbon dioxide under fuel cell operating conditions*, Journal of the Electrochemical Society, 164, F1063-F1073, 2017.
31. S. Suzuki, H. Muroyama, T. Matsui, K. Eguchi, *Influence of CO<sub>2</sub> dissolution into anion exchange membrane on fuel cell performance*, Electrochimica Acta, 88, 552-558, 2013.
32. H. Yanagi, K. Fukuta, *Anion exchange membrane and ionomer for alkaline*

- membrane fuel cells (AMFCs)*, ECS transactions, 16, 257-262, 2008.
33. I. Gunasekara, M. Lee, D. Abbott, S. Mukerjee, *Mass Transport and Oxygen Reduction Kinetics at an Anion Exchange Membrane Interface: Microelectrode Studies on Effect of Carbonate Exchange*, ECS Electrochemistry Letters, 1, F16-F19, 2012.
34. V. J. Bharath, J. R. Jervis, J. J. Bailey, E. Engebretsen, T. P. Neville, J. Millichamp, T. Mason, P. R. Shearing, R. J. C. Brown, G. Manos, D. J. L. Brett, *Effect of humidity on the interaction of CO<sub>2</sub> with alkaline anion exchange membranes probed using the quartz crystal microbalance*, International Journal of Hydrogen Energy, 42, 24301-24307, 2017.
35. L. A. Adams, S. D. Poynton, C. Tamain, R. C. T. Slade, J. R. Varcoe, *A carbon dioxide tolerant aqueous-electrolyte-free anion-exchange membrane alkaline fuel cell*, ChemSusChem, 1, 79-81, 2008.
36. Y. Katayama, K. Yamauchi, K. Hayashi, T. Okanishi, H. Muroyama, T. Matsui, Y. Kikkawa, T. Negishi, S. Watanabe, T. Isomura, K. Eguchi, *Anion-exchange membrane fuel cells with improved CO<sub>2</sub> tolerance: Impact of chemically induced bicarbonate ion consumption*, ACS Applied Materials & Interfaces, 9, 28650-28658, 2017.
37. W. Sheng, A. P. Bivens, M. N. Z. Myint, Z. Zhuang, R. V. Forest, Q. Fang, J. G

- Chen, Y. Yan, *Non-precious metal electrocatalysts with high activity for hydrogen oxidation reaction in alkaline electrolytes*, Energy & Environmental Science, 7, 1719-1724, 2014.
38. Y. Wang, G. Wang, G. Li, B. Huang, J. Pan, Q. Liu, J. Han, L. Xiao, J. Lu, L. Zhuang, *Pt–Ru catalyzed hydrogen oxidation in alkaline media: oxophilic effect or electronic effect?*, Energy & Environmental Science, 8, 177-181, 2015.
39. D. Strmcnik, M. Uchimura, C. Wang, R. Subbaraman, N. Danilovic, D. Vliet, A. P. Paulikas, V. R. Stamenkovic, N. M. Markovic, *Improving the hydrogen oxidation reaction rate by promotion of hydroxyl adsorption*, Nature Chemistry, 5, 300-306, 2013.
40. H. A. Miller, A. Lavacchi, F. Vizza, M. Marelli, F. D. Benedetto, F. D’Acapito, Y. Paska, M. Page, D. R. Dekel, *A Pd/C-CeO<sub>2</sub> anode catalyst for high-performance platinum-free anion exchange membrane fuel cells*, Angewandte Chemie, 128, 6108-6111, 2016.
41. J. Durst, A. Siebel, C. Simon, F. Hasch e, J. Herranz and H. A. Gasteiger, *New insights into the electrochemical hydrogen oxidation and evolution reaction mechanism*, Energy & Environmental Science, 7, 2255-2260, 2014.
42. H. T. Chung, U. Martinez, I. Matanovic, Y. S. Kim, *Cation–hydroxide–water coadsorption inhibits the alkaline hydrogen oxidation reaction*, The Journal of Physical Chemistry Letters, 7, 4464-4469, 2016.

# **Chapter 2 Engineering the MEA parameters for Improving the Performance of AEMFCs with Platinum Cathode Catalyst**

Some parts have been reedited from published results entitled “A Facile Approach to Improve the Performance of Alkaline Anion Exchange Membrane Fuel Cells by Reducing Ionic Resistance”, J. Ind. Eng. Chem., 2017.

## **2.1 Introduction**

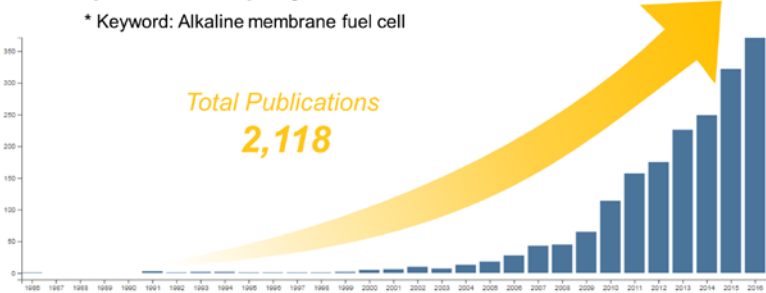
Anion exchange membrane fuel cells (AEMFCs) are an alternative to PEMFCs, which have gained much attention in recent years. The most notable advantage of AEMFC is its ability to use inexpensive materials for catalysts due to high pH operating conditions<sup>1</sup>. Although numerous research has reported excellent performance of their synthesized catalysts compared to Pt in the half-cell system, this does not always mean it will be superior in the case of single-cell system<sup>2-5</sup>. To overcome the challenges with different trends of performance between single-cell and half-cell systems, the optimization of the MEA condition should be prioritized.

MEA is the critical component of the single-cell system of polymer electrolyte membrane fuel cells (PEMFCs), which is composed of a gas diffusion

layers (GDLs), polymer electrolyte membrane, and catalyst layers. The performance of the single-cell is determined by the properties of each component of the MEA rather than the intrinsic activity of the catalyst itself. PEMFCs with a system similar to AEMFCs have been greatly improved through the study of MEA. By using carbon supported Pt instead of Pt black as the catalyst, the amount of catalyst loading is reduced by 90 % and the catalyst layer thickness also decreased<sup>6</sup>. Furthermore, by impregnating the interstitial spaces between catalyst particles with proton conducting material (i.e. Nafion as an ionomer), the performance improved by more than 16 times than before<sup>7</sup>. To date, more than 2000 research papers on alkaline fuel cells have been published and have recorded up to 4000 citation counts (Figure 2.1). Despite the importance of membrane-electrode-assembly (MEA) to improve the performance of fuel cells, papers that studied in terms of MEA make up only 3 % of the total publications on AEMFCs. Understanding the parameters that control the performance of MEA is of critical importance for realizing high performance of AEMFCs.

The main parameters that determines the performance of MEA are considered to be ionic conduction and mass transport in the catalyst layer. The properties of the polymer electrolyte and the catalyst layer hydration, which is controlled by precise adjustments on the fabricating MEA and operating conditions, are the important for the high ionic conductivity in the electrode<sup>8,9</sup>. In this respect, mass

❖ Number of publications per year



❖ Number of citations per year

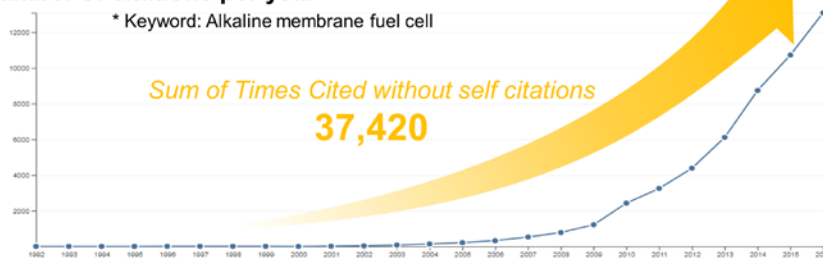


**Figure 2.1** Number of publications and citations per year about AEMFCs

transport and ionic conduction are closely correlated. Particularly, the ratio of the catalyst layer thickness to the membrane thickness is higher in AEMFCs than in PEMFCs<sup>10</sup>, therefore the ionic conductivity and mass transport in the catalyst layer can account for a larger portion of the performance than in PEMFCs case. In particular, for AEMFCs, water is not only the product at the anode side as a result of hydrogen oxidation reaction (HOR), but also the reactant for oxidation reduction reaction (ORR) at the cathode side. Therefore, water management is a tricky task but also very important especially in terms of ionic and concentration overpotential. Water should be evenly distributed within the catalyst layer for high ion conductivity and ORR but should not block the reaction site and gas transport path of GDL.

In this chapter, I investigated the effect of MEA parameters on performance through the AEMFCs using a platinum catalyst cathode. First, the pretreatment method for activating the MEA is suggested for reducing their ohmic overpotentials in the catalyst layer. Subsequently, the effect of the catalyst layer structure on the performance of AEMFCs was investigated using catalyst ink solvents with different dielectric constants. Finally, the GDL properties were changed to optimize water management.

## 2.2 Experimental

### 2.2.1 Materials Preparation

#### Preparation of MEAs

The catalysts powder, commercial ionomers (*Different types of ionomers have been used for each part of this thesis due to the problem of supply from the manufacturers*) and solvents were mixed and sonicated. An in-house pore-filling membrane was used. Before the deposition of catalyst layer onto the membrane, all the membranes were immersed in 1M KOH solution and rinsed in deionized (DI) water to remove excess OH<sup>-</sup> ions and other ions from the KOH solution. The homogenized catalyst inks were deposited onto the membrane by the spraying method. The catalyst loading of Pt/C 40 wt% and the synthesized non-precious metals catalyst (NPMC) were 0.5 mg cm<sup>-2</sup> and 2 mg cm<sup>-2</sup>, respectively. The anode used for all AEMFC tests in this work was Pt/C 40 wt% with a load of 0.5 mg cm<sup>-2</sup>. The fabricated catalyst coated membranes (CCM) were dried for 1 day in air before testing. The CCM was immersed in 1 M KOH solution for 1 hour and then rinsed with DI water to remove excess OH<sup>-</sup> and other ions that may have been present on the electrode and on the membrane. Four different types of Carbon papers were used as a gas diffusion layer and placed next to the CCMs (detailed properties of carbon papers are described in 2.3.3). The active electrode area was 5 cm<sup>2</sup>.

## **2.2.2 Characterizations and Electrochemical Test**

### **Characterization techniques**

The field-emission scanning electron microscopy (FE-SEM, MERLIN Compact, ZEISS) and energy-dispersive X-ray spectroscopy (EDX, SU70, Hitachi) were used to characterize the morphology and chemical properties of the electrode and the anion exchange ionomer. FT-IR spectroscopy (Nicolet 6700, Thermo Scientific) was performed in attenuated total reflectance (ATR) mode. For the analysis of the ionomer by FT-IR and EDX spectroscopy, solidified ionomer was prepared by casting ionomer solution onto a silicon wafer. The size of ionomer agglomerates in the various solvents were measured by an electrophoretic light scattering spectrophotometer (ELS Z-1000, Otsuka Electronics). Mercury porosimetry (Micro Active AutoPore V 9600, Micromeritics) was used to investigate the pore size of the carbon papers. The water contact angles of the carbon papers were measured using a contact angle analyzer (Phoenix-300 Touch, S.E.O)

### **Electrochemical analysis**

The performance of AEMFCs was tested using the fuel cell test system (CNL energy Co.). Humidified hydrogen and oxygen gases were fed to the anode and cathode sides of a single-cell, respectively, at a constant flow while operating the

single-cell. For the decarbonation within the cell, a constant voltage at 0.1 V was applied to the single-cell before the test. Polarization curves were measured using a current-sweep method with a rate of  $10 \text{ mA cm}^{-2} \text{ s}^{-1}$  while maintaining the cell temperature at  $50^\circ\text{C}$ . While operating fuel cells, the total outlet pressures were 150 kPa and atmospheric pressure for NPMC and Pt/C, respectively. Electrochemical impedance spectroscopy (EIS) was performed in galvanostatic mode at a constant current with an amplitude of 5 % of the constant current in the range from 10 mHz to 100 kHz. To compare the ionic resistance in the cathodes, humidified hydrogen and nitrogen gases were supplied to the anode and cathode, respectively. The temperature of the cell was maintained at  $30^\circ\text{C}$ . The applied cell voltage was 0.45 V under a non-faradaic reaction with frequency ranging from 10 mHz to 100 kHz.

## 2.3 Results and Discussion

### 2.3.1 Activation Method

The single-cell results of DI- and KOH-treated MEA using AEMFC are shown in Figure 2.2. The performance of KOH-treated MEA exhibited higher performance than that of DI-treated MEA. The maximum power densities were 198 and 264 mW cm<sup>-2</sup> for the DI- and KOH-treated MEA, respectively. The difference between the polarization curves of the DI- and KOH-treated MEA was observed in the intermediate current density region, where the ohmic resistance is the dominant factor governing the performance of single-cell<sup>11</sup>. The membranes used for both MEAs were treated with KOH solution before depositing the catalyst layer onto it. Hence, the difference in performance between KOH- and DI-treated MEAs is attributed to the difference in the catalyst layer property, especially the ionomer state. The open circuit voltages (OCV) were similar because the catalyst and its loading amount were identical for both MEAs. Therefore, catalyst layer thickness of the DI- and KOH-treated MEAs were almost same (~14 µm) as can be observed in the cross-sectional FE-SEM images in Figure 2.3. Thus, in the low current density region, where the voltage loss is mainly affected by the activation overpotential<sup>12</sup>, the polarization curves for the two MEAs were similar to each other. The higher performance of KOH-treated MEA

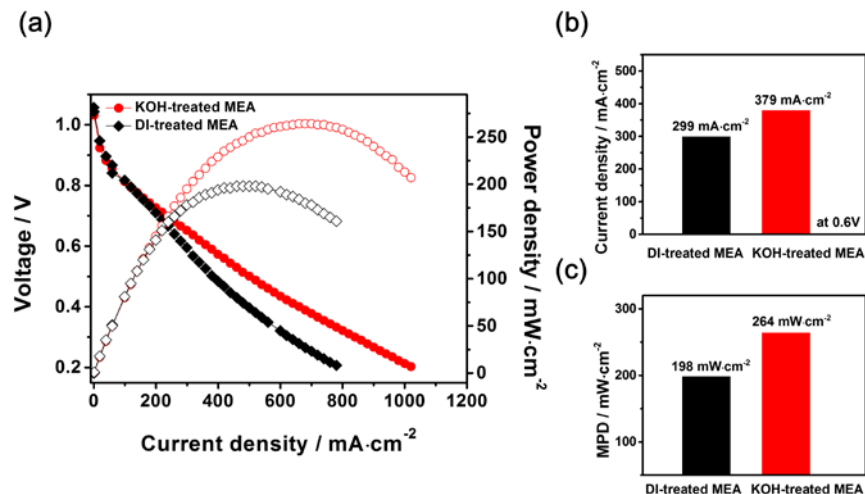


**Figure 2.2** (a) Polarization (●) and power density (○) curves of Pt/C catalyst, (b) current density at 0.6 V and (c) maximum power density of single-cells with DI- and KOH- treated MEAs.

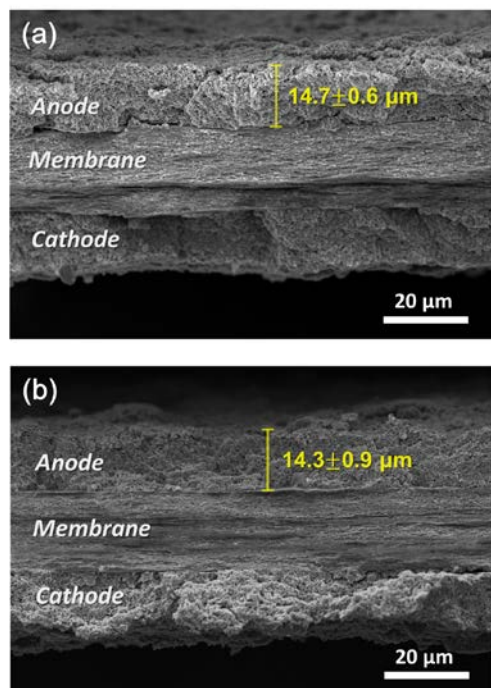
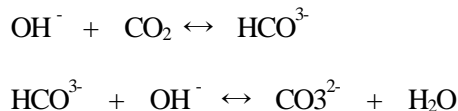


**Figure 2.3** Cross sectional FE-SEM images of (a) DI- and (b) KOH-treated MEAs.

at intermediate current density is attributed to the replacement of  $\text{Cl}^-$  to  $\text{OH}^-$ , leading to decrease in ohmic resistance because the ionic conductivity of  $\text{OH}^-$  was more than twice that of  $\text{Cl}^-$ <sup>13, 14</sup>. To demonstrate the reason for the enhanced performance, the changes in ionomer properties were analyzed by EDX and FT-IR spectroscopy.

To confirm the presence of  $\text{Cl}^-$  as the counter anion in the ionomer, EDX analysis was conducted with the solidified anion exchange ionomer (Figure 2.4(a)). The signal corresponding to  $\text{K}\alpha$  of  $\text{Cl}^-$  peak is clearly observed in the EDX spectrum of DI-treated solidified ionomer at around 2.6 keV. The atomic (weight) percentage of  $\text{Cl}^-$  in the ionomer was decreased from 1.90 % (5.21 %) to 0.07 % (0.21 %) after KOH treatment. The observed Si peak near 1.7 keV is from the substrate. A comparison of the hydroxide peak in the FT-IR spectra of KOH- and DI-treated solidified ionomers supports the replacement of  $\text{Cl}^-$  to  $\text{OH}^-$  (Figure 2.4(b)). Wide  $\text{OH}^-$  absorption peak at 3716–3050  $\text{cm}^{-1}$  was only observed in the spectrum of the KOH-treated solidified ionomer. This result is consistent with EDX data and indicates that  $\text{Cl}^-$  was successfully replaced with  $\text{OH}^-$  through the KOH treatment. The absorption peak at 1660–1537  $\text{cm}^{-1}$ , corresponding to the C=O groups, were only detected in KOH-treated solidified ionomer. This could be due to the carbonization of some portion of the substituted  $\text{OH}^-$  to  $\text{CO}_3^{2-}$  or  $\text{HCO}_3^{3-}$  while drying the solidified ionomer to remove the water contained in it. It is

generally known that  $\text{OH}^-$  in the AEM reacts with  $\text{CO}_2$  when the air supply to the cathode side and converted to  $\text{HCO}^{3-}$  as shown in the following reaction equations<sup>15</sup>.



Therefore, the observed C=O group peaks can be considered to be the evidence for the existence of  $\text{OH}^-$  in the KOH-treated solidified ionomer.

To clarify the reason for ohmic overpotential difference between the two MEAs, EIS analysis of the MEAs should be performed. EIS for the faradaic condition was performed in galvanostatic mode under single-cell operating conditions to keep the same amount of water in the catalyst layer. Figure 2.5 shows Nyquist plots measured at a current of -2 A, where the ohmic resistance is the dominant cause for the loss in cell potential. For porous electrode, the high-frequency intercept on the real impedance axis corresponds to the sum of the ionic resistance of membrane and ohmic resistance, which in turn is attributed to the ionic and electronic resistance through the catalyst layer, and the diameter of the semicircle represents the charge transfer resistance of reaction<sup>16</sup>. The impedance spectra showed a reduction in ohmic and charge transfer resistances after KOH treatment. At this point on the spectra, the ionic resistance of the membrane and

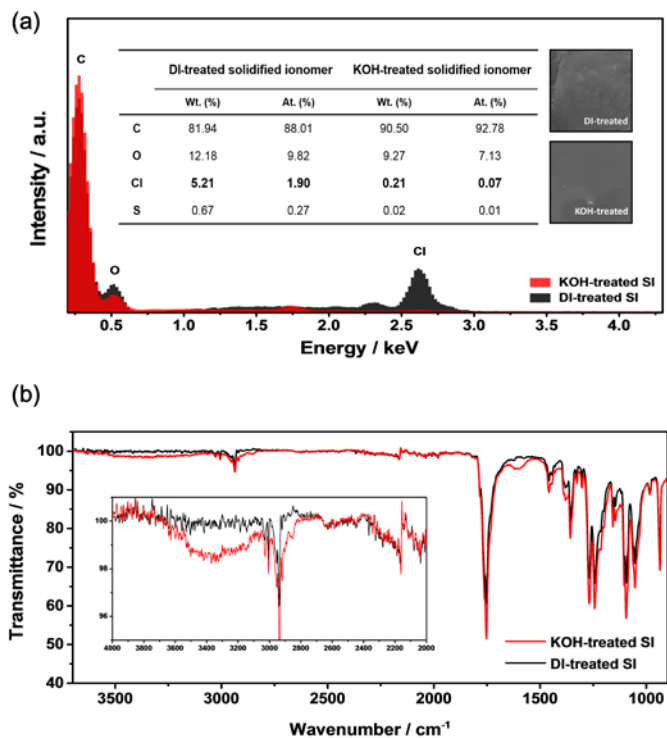


**Figure 2.4** (a) EDX spectrum and (b) FT-IR spectrum of solidified ionomer after DI and KOH treatments.

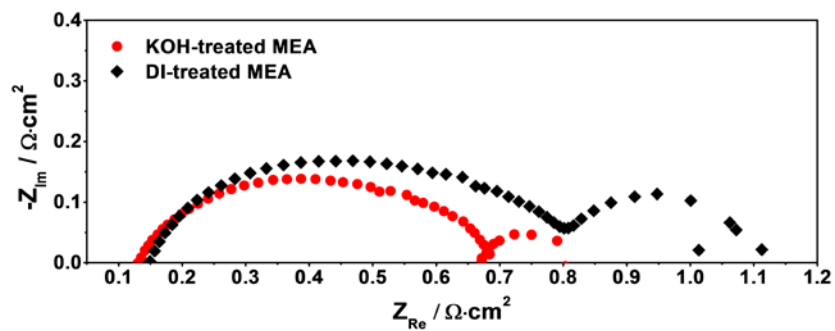


**Figure 2.5** Nyquist impedance plots of the DI- and KOH-treated MEAs for H<sub>2</sub>/O<sub>2</sub> operation at constant current of −2 A.

electronic resistance of the catalyst layer, should be similar for both MEAs, suggesting that the reduction in ohmic resistance is due to the decrease in ionic resistance through the catalyst layer.

To further demonstrate the improvement in ionic resistance for hydroxide conduction in the cathode catalyst layer, EIS analysis was performed under the non-faradaic condition for the cathode. Although several studies have used EIS analysis to investigate ionic resistance in PEMFCs<sup>17,18</sup>, there have been few reports on the EIS-based analysis of ionic resistance in AEMFCs. Generally, equivalent circuit of catalyst layers can be represented by the transmission line model shown in Figure 2.6 (a)<sup>19,20</sup>. The impedance of the catalyst layer is composed of ionic ( $R_i$ ) and electronic resistances ( $R_e$ ) due to ion conduction through the ionomer networks and electron conduction through the catalyst particles, respectively. The interfacial reaction impedances ( $Z$ ) at the triple phase boundaries are distributed in the catalyst layers. When inert nitrogen is supplied to the cathode side, the faradaic reactions are removed. Thus, the interfacial reaction impedances can be considered as a simple capacitor. The equivalent circuit of cathode catalyst layer under this experimental condition is shown in Figure 2.6 (b), assuming that the electronic resistance is negligible.

The Nyquist plots of impedance spectra of two MEAs are shown in Figure 2.7 (a), which was measured while hydrogen and nitrogen gases were supplied to the

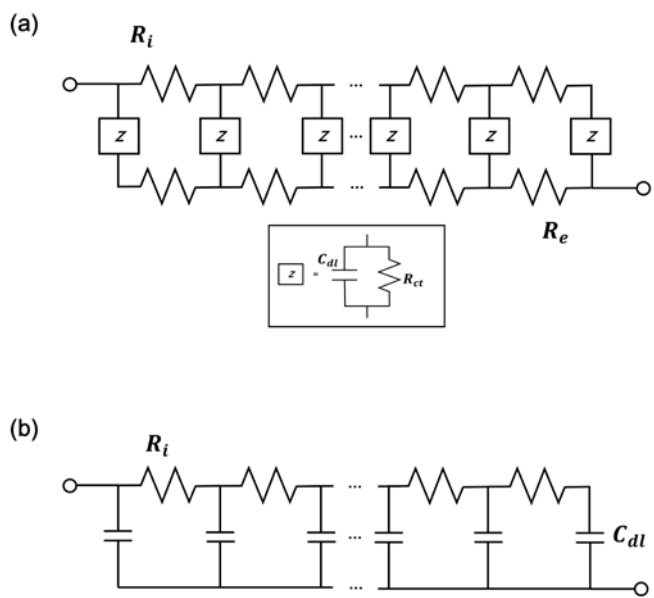


**Figure 2.6** Equivalent circuit for the impedance of the catalyst layer of fuel cell

under (a) the faradaic condition and (b) non-faradaic condition.

anode and cathode, respectively. In the high-frequency range, an arc with the shape of a quarter-circle was observed for both the MEAs, which is due to the hydrogen oxidation reaction (HOR). Since exchange current density of HOR under alkaline condition is not negligible compared to that of oxygen reduction reaction, the impedance of HOR observed for AEMFCs differed from that of PEMFCs. Charge transport resistance for HOR was decreased, as confirmed by the smaller size of quarter-circle of KOH-treated MEA, which is consistent with the results shown in Figure 2.5. The ionomer networks through the catalyst were improved by the KOH treatment, which in turn leads to a decrease in the charge transport resistance. Under the non-faradaic condition of the cathode catalyst layer, interfacial capacitors are distributed with ionic resistance. (Figure 2.7 (b)). In this case, the slope of the Nyquist plot should be changed sharply from 45° to 90°. However, in here, the slope gradually changed due to non-uniform microstructure of catalyst layer<sup>18</sup>. A comparison of the impedance of two MEAs (Figure 2.7 (a)) showed that the KOH-treated MEA has the lower ionic resistance. To obtain the quantitative data of ionic resistance, the experimental impedance data ( $Z(f)$ ) is further converted to complex capacitance ( $C_c(f)$ ), according to equation (1), where  $f$  denotes the AC frequency. Real and imaginary parts of the complex capacitance were plotted as a function of AC frequency. Low-frequency intercept on the real capacitance axis in Figure 2.7 (b) is the total capacitance of the cathode catalyst

layer ( $C_{dl}$ ). From peak frequency in the imaginary capacitance plot (Figure 2.7 (c)),  $R_i$  and  $C_{dl}$  can be calculated using equation (2)<sup>19,20</sup>. Based on this relationship,  $R_i$  values of KOH- and DI-treated MEA are calculated to be  $3.135 \Omega \cdot \text{cm}^2$  and  $7.941 \Omega \cdot \text{cm}^2$ , respectively. Thus, ionic resistance in the catalyst layer has declined by about half after the KOH treatment.

$$C_c(f) = 1/j2\pi f Z_c(f) = C_{dl}/(j2\pi R_i C_{dl} f)^{1/2} \tanh[(j2\pi R_i C_{dl} f)^{1/2}] \quad (\text{Eq. 1})$$

$$A = \int_{-\infty}^{\infty} Im[c_c(f)] d \log f = 0.682 C_{dl}$$

$$f_p = 0.404/R_i C_{dl} \quad (\text{Eq. 2})$$

This method was applied to carbon-based NPMC<sup>21</sup>. Figure 2.8 (a) shows the cell performance of NPMC with a catalyst loading of  $2 \text{ mg cm}^{-2}$ , which indicates that a higher loading of catalyst layer is required for NPMC when compared to a commercial Pt/C catalyst ( $0.5 \text{ mg cm}^{-2}$ ). The maximum power density of an AEMFC with KOH-treated MEA approaches  $169 \text{ mW cm}^{-2}$ , which is 2.4 times higher than that of the DI-treated MEA ( $72 \text{ mW cm}^{-2}$ ). In this case, there is a clear enhancement of performance observed in the intermediate current density region. The higher performance improvement ratio of MEA with NPMC to PGM catalyst after KOH treatment is due to the increased thickness of NPMC catalyst layer, as observed in Figure 2.8 (b). This clearly suggests that the enhancement of  $\text{OH}^-$

conductivity of ionomer in the catalyst layer could immensely contribute to the single-cell performance, which in turn is accomplished due to a higher proportion of catalyst layer on MEA.

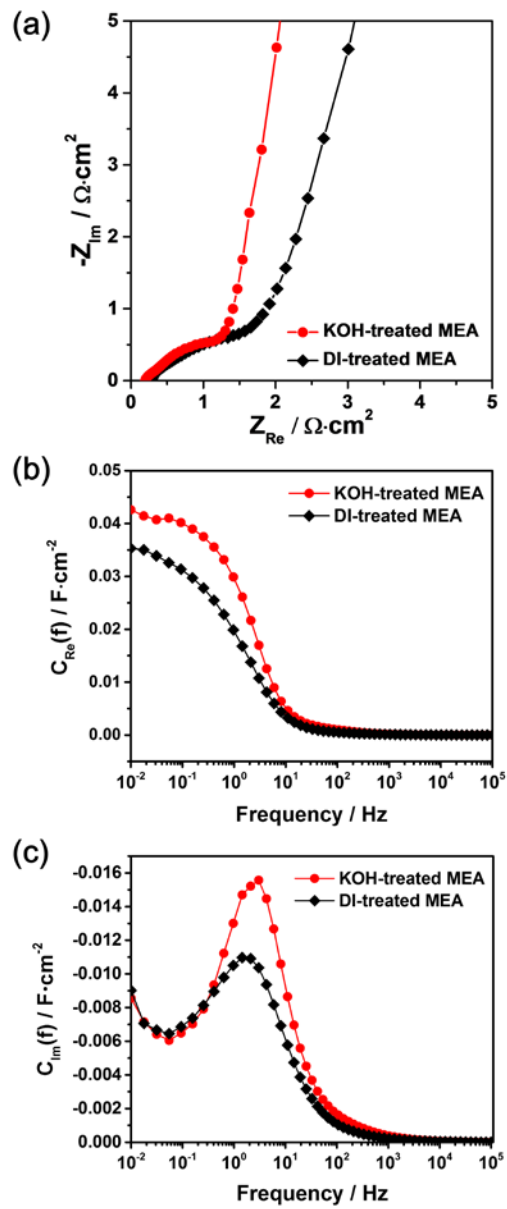


**Figure 2.7** (a) Nyquist impedance plots, (b) real part and (c) imaginary part of complex capacitances as a function of log scale frequency of the DI- and KOH-treated MEAs for  $\text{H}_2/\text{N}_2$  operation at 0.45 V.

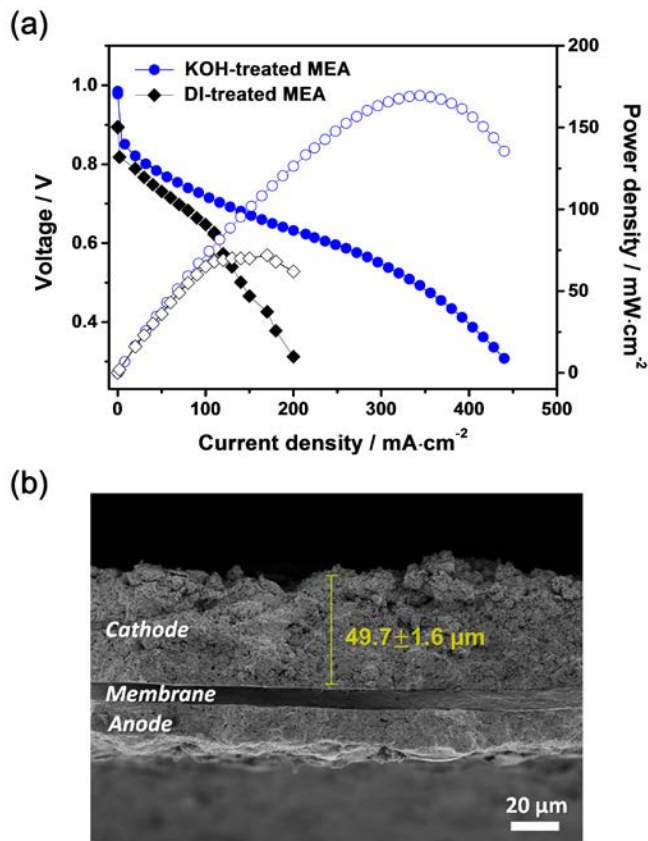


**Figure 2.8** (a) Polarization (●) and power density (○) curves and (b) FE-SEM cross sectional FE-SEM image of MEA with NPMC.

### **2.3.2 Effect of Catalyst Ink Solvents**

In order to confirm the interaction between the ionomer and solvent with distinct dielectric constant, the average ionomer agglomerates size dispersed in solvent was measured by an electrophoretic light scattering (ELS) particle size analyzer (Figure 2.9). The physical properties of these solvents are listed in Table 2.1. The effect of the solvent on the size of the ionomer agglomerate is remarkable. As dielectric constant increases from 12.5 to 24.6, the average agglomerate size decreases markedly from 160 nm to 20 nm, which is attributed to different interactions with the side chain and back bone of ionomer in solvent<sup>22-24</sup>. The change in the size of the ionomer agglomerates depending on the solvent can be observed in an optical micrograph of solution (inset images of Figure 2.9). The ionomer dispersed state is not completely identical to the case of when the carbon supported catalyst particles coexist with the ionomer in solution, but the effect of the solvent on the ionomer with different dielectric constants is clearly confirmed. The effect on the type of catalyst dispersion solvent for practical conditions was evaluated using AEMFC single-cell analysis with MEA prepared with solvents having different dielectric constants. Figure 2.10 shows the SEM images of prepared catalyst layers. The noticeable difference of the pore structure in the catalyst layer is observed in the SEM images. Catalyst layer originated from tert-butanol shows well-developed

secondary pore structure with a large size. In contrast, when using ethanol with a high dielectric constant, the catalyst layer presents a fine and dense microstructure. As the dielectric constant of the solvent decreases, the catalyst agglomerate size increases due to the increase of the ionomer agglomerate size, which remarkably enlarges the size of the secondary pores in the catalyst layers. These results indicates correlation between the ionomer agglomeration and the catalyst layer porous structure.

The performance test results of AEMFCs are shown in Figure 2.11. The MEAs prepared from the solvents with lower dielectric constant exhibited higher performance. The best performance was observed in AEMFC prepared with catalyst dispersed in tert-butanol. The gaps between the polarization curves mainly occur at a current density region where the cell voltage loss is dominated by ohmic and concentration loss<sup>11,12</sup>. This result is attributed to the large secondary pore sizes, which originate from stronger agglomeration property of ionomer in a tert-butanol solvent, facilitating mass transfer through the catalyst layer. The enhancement of the mass transport is also confirmed by the oxygen gain, calculated by subtracting voltage obtained from oxygen-fed fuel cell to air-fed fuel cell. As seen in Figure 2.11 (c), the AEMFC prepared from tert-butanol solvent showed a much lower oxygen gain compared to one prepared from solvents with higher dielectric constant, indicating that the tert-butanol originated catalyst layer has a more

**Table 2.1** Physical parameters of various dispersion solvents.

Solvent	Boiling point	Dielectric constant
<b>tert- Butanol</b>	82.4	12.5
<b>2-Propanol</b>	82.4	18.3
<b>Ethanol</b>	78.5	24.6

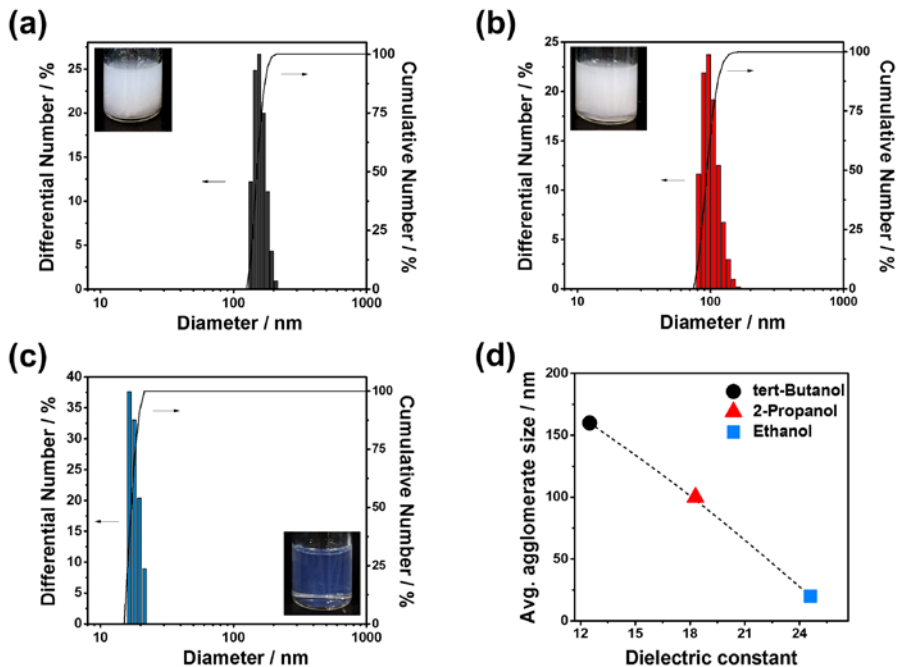


**Figure 2.9** The size distribution of ionomer agglomerates dispersed in the (a) tert-butanol, (b) 2-propanol and (c) ethanol. Inset images are an optical micrograph of ionomer dispersion. (d) Average size of ionomer aggregates in accordance to solvents with different dielectric constants.

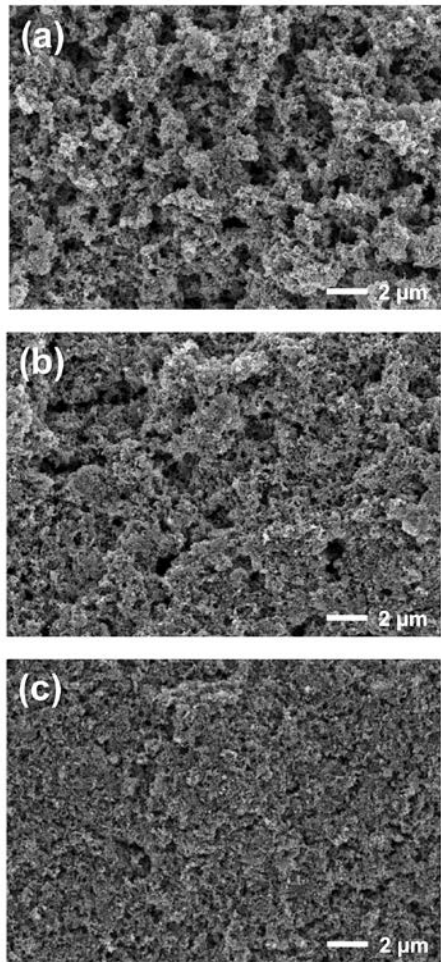


**Figure 2.10** SEM images of the catalyst layer structure fabricated with different catalyst dispersion solvent. (a) tert-butanol, (b) 2-propanol and (c) ethanol solvents.

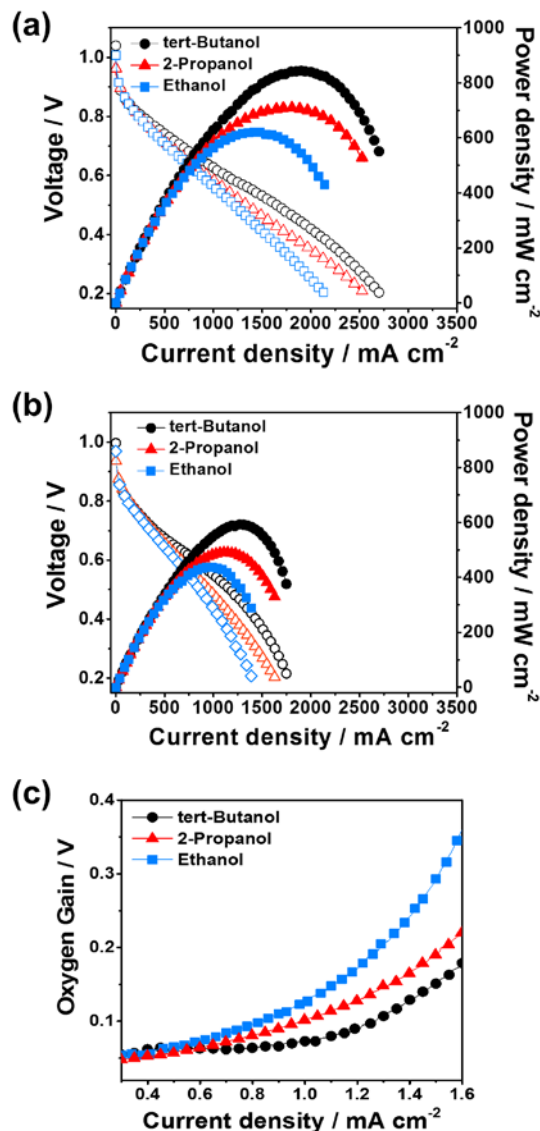


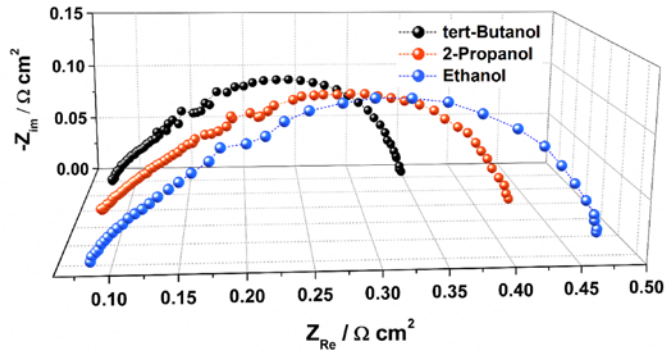
**Figure 2.11** Polarization curves of AEMFCs using MEAs prepared with different catalyst dispersion solvents under the conditions of (a) H<sub>2</sub>/O<sub>2</sub> and (b) H<sub>2</sub>/Air. (c) Oxygen gain as a function of current density.

favorable pore structure for facile mass transport<sup>25,26</sup>. To further investigate the effect of dielectric constant of solvent on the performance, EIS analysis of the MEAs for the faradaic condition were carried out in galvanostatic mode under single-cell operating conditions to keep the same amount of water. Figure 2.12 presents Nyquist plots of AEMFCs measured at different current densities according to the different dominant voltage loss. As observed at all the current densities, the ohmic resistance of the AEMFC prepared from tert-butanol is slightly less than that of the AEMFC prepared from 2-propanol and ethanol, indicating the lower ionic resistance at the interface of membrane and catalyst layer. The nyquist plot (Figure 2.12 (a)) measured at -1 A, the diameter of the semicircle decreases with decreasing the dielectric constant of solvents, indicating the reduced activation overpotential resulted from the higher reactant concentration due to the advantageous mass transfer structure in the catalyst layer<sup>27</sup>. As can be seen in the nyquist plot measured at -10 A (Figure 2.12 (c)), the highest concentration overpotential was observed in the AEMFC prepared from ethanol, which is caused by mass transfer resistance. These results are also consistent with the polarization curves (Figure 2.11 (a)) because the impedance diameters are proportional to the polarization curves. To clarify the effect of solvent dielectric constant on ionic conduction in the electrode, the nyquist plots were measured at open-circuit voltage (OCV) corresponding to non-faradaic

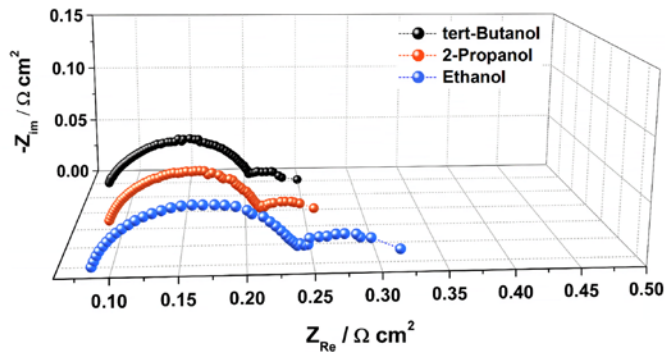
condition. In Figure 2.13, the difference in ionic resistance was clearly observed. It was confirmed that the ionic resistance increases with the increase of the dielectric constant, which is also supported by the nyquist plot results measured at -5 A (Figure 2.12 (b)).

Thus, the best performance of the AEMFC prepared from tert-butanol was attributed its favorable porous structure, which facilitates the transport of humidified gas and products in the catalyst layer, leading to the reduced ionic and mass transfer resistance.

(a)



(b)



(c)

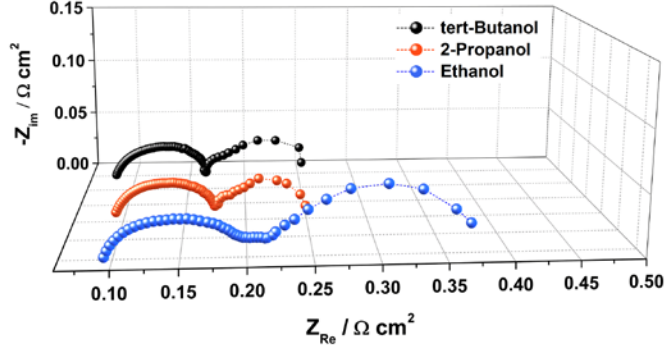


**Figure 2.12** Nyquist impedance plots of AEMFCs using MEAs prepared with different catalyst dispersion solvents for  $\text{H}_2/\text{O}_2$  operation at constant current of (a) -1 A, (b) -5 A and (c) -10 A.

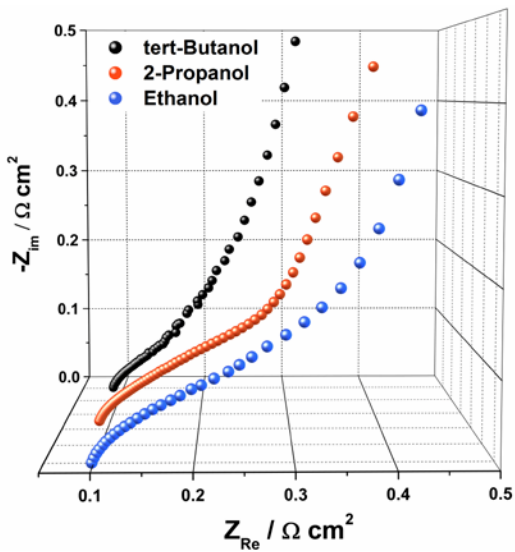


**Figure 2.13** Nyquist impedance plots of AEMFCs using MEAs prepared with different catalyst dispersion solvents for H<sub>2</sub>/N<sub>2</sub> operation at open-circuit voltage.

### **2.3.3 Effect of Gas Diffusion Layer Properties**

In a polymer electrolyte fuel cell, water management is crucial for stability and high performance. There are two main transportation modes for water inside the MEA; electro-osmotic drag by counter ion and back diffusion by water gradient<sup>28,29</sup>. In AEMFCs, water management is more complicated than PEMFCs. This is because water is a product of the hydrogen oxidation reaction and simultaneously a reactant for oxygen reduction reaction during cell operation. Water is moved from anode to cathode with hydroxide ion by electro-osmotic drag. In the opposite way, water also can be moved from cathode to anode by back diffusion, because of the water gradient as a result of water being generated at the anode side because of hydrogen oxidation reaction (HOR). The dominant direction of water could be governed by membrane properties; if the membrane is hydrophilic then back diffusion will be main water transport mode. In contrast, in a hydrophobic membrane, water would be difficult to diffuse from the anode to cathode so the electro-osmotic drag will be the dominant water transport mode<sup>30</sup>. For better water management, water movement property in homemade anion exchange membrane (AEM) used for this study was confirmed by a simple experiment. The detailed test conditions are shown in Table 2.2. The cell was operated in galvanostatic mode at constant current -3 A. There are four types of water; injecting

**Table 2.2** Operating parameters

Properties	Unit	Value
Cell temperature	°C	50
Anode humidifier temperature	°C	45
Cathode humidifier temperature	°C	50
Anode gas flow rate	ml/min	800
Cathode gas flow rate	ml/min	1000
Applied current	A	-3

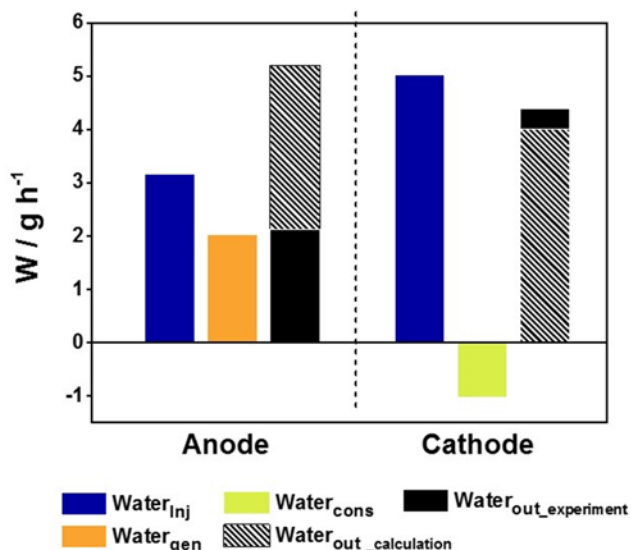
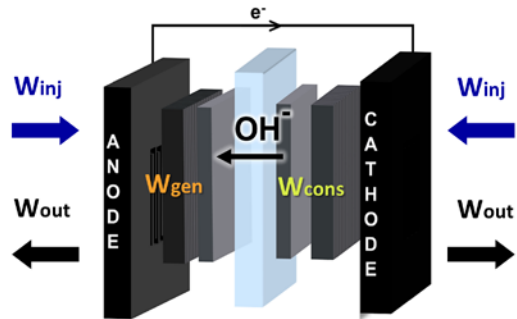


**Figure 2.14** The amount of water detected and calculated according to the HOR

and ORR at each side of electrode at constant current -3A.

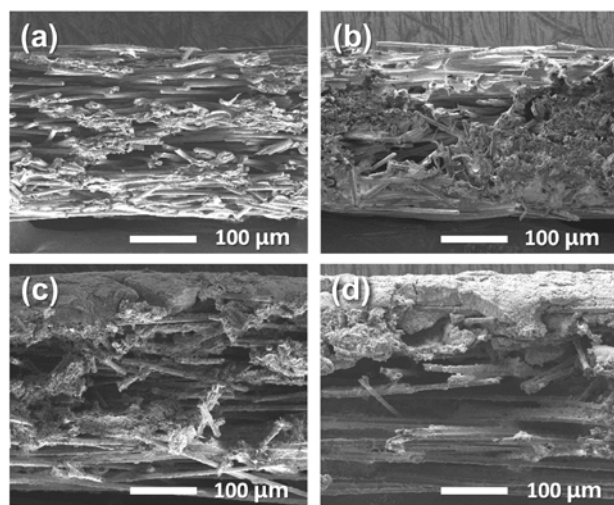
water at each side inlet through the humidified gas,  $W_{inj}$ , generated water by HOR,  $W_{gen}$ , consumed water by ORR,  $W_{cons}$ , water trapped from the outlet of each side electrode,  $W_{out}$ . The calculated  $W_{out}$  was expected to be higher on the anode side than on the cathode side. But the results show that  $W_{out,c}$  was almost twice as high as  $W_{out,a}$  as shown in Figure 2.14. This indicates that water dominantly moves from anode to cathode and that back diffusion is the dominant mode for water transportation in this case. To facilitate the oxygen reduction reaction by supplying adequate water into the cathode side, the movement of water from the anode to the cathode side should be promoted. Controlling the properties of the gas diffusion layers (GDLs) is part of an attempt to promote the back diffusion of water inside the cell. The GDLs consist of a macroporous substrate (generally carbon paper, carbon cloth) and a mesoporous layer (MPL) deposited on top of it as needed. Macroporous substrate serves as a gas distributor and current collector and MPL reduces contact resistance between the catalyst layer (CL) and macroporous substrate with its compact carbon layer and controls the water movement<sup>31</sup>. In this study, to improve the performance of AEMFCs, the effect of the presence of the MPL layer and the degree of hydrophobicity of GDLs on the performance of AEMFCs were investigated. The physical properties of GDL used in this study are given in Table 2.3. GDL composed of carbon paper without MPL layer (CP and CP H) and GDLs with MPL layer on carbon paper (CPM L, CPM H) were

**Table 2.3** The physical properties of GDLs

	CP Carbon paper	CP H Carbon paper + PTFE	CPM L Carbon paper + mesoporous layer + PTFE	CPM H Carbon paper + mesoporous layer + PTFE
<b>Thickness / <math>\mu\text{m}</math></b>	280	280	320	320
<b>Pore size / <math>\mu\text{m}</math></b>	1.82	1.66	0.64	0.44
<b>Water Contact Angle / <math>^\circ</math></b>	125	137	139	141

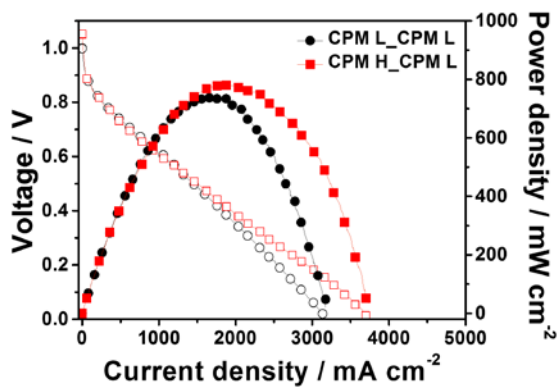
used. Here, the hydrophobicity of GDLs was controlled, thus 4 types of GDLs were used for this experiment. L and H denote less hydrophobic and more hydrophobic, respectively. In order to focus on the effect of pore size and hydrophobicity of GDLs, the thickness of GDLs is set to be as similar as possible, and the thickness of each electrode is in the range of 280 ~ 320  $\mu\text{m}$ . After incorporating PTFE as a hydrophobic agent into the carbon paper to increase the hydrophobicity, a decrease in pore size is observed, which can also be seen in the SEM cross-sectional image (Figure 2.15). Thus, it was confirmed that CP H has a larger water contact angle than CP. In the case of GDL containing MPL, the average pore size decreases to about half of that of CP due to the deposition of MPL, CPM H has the smallest pore size and more hydrophobic characteristics.

Figure 2.16 (a) exhibits the polarization curves of the AEMFCs measured using the two different GDLs types. GDLs containing MPL with different hydrophobicity was applied to the anode. It is generally known that it is effective to introduce MPL to prevent flooding on the side where water is generated as confirmed in PEMFC system<sup>32-34</sup>. The limiting current density increased by 20 % when CPM H was used. This is because more hydrophobic and small pore CPM H facilitates back diffusion of water from the anode through the membrane with a stronger capillary force, thereby promoting the cathode reaction rate and improving ionic conductivity<sup>29</sup>. It was also confirmed by the reduced ohmic overpotential of the



**Figure 2.15** Cross sectional FE-SEM images of four different type of GDLs; (a) CP, (b) CP H, (c) CPM L and (d) CPM H.

(a)



(b)

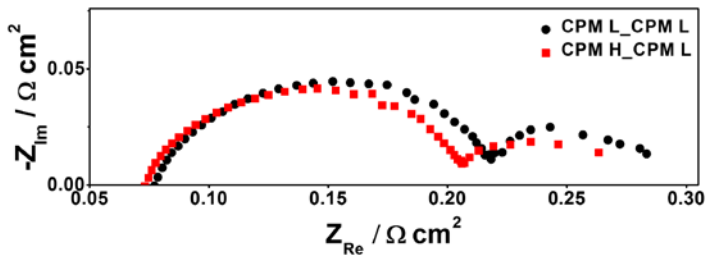


**Figure 2.16** (a) Polarization curves and (b) Nyquist plots of AEMFC using CPM L and CPM H as the anode GDLs and CPM L as the cathode GDLs.  
(Nyquist plot measured at -5 A)

AEMFC using CPM H as the anode GDL (Figure 2.16 (b)). The effect of the properties of cathode GDL on the AEMFC performance is shown in the Figure 2.17. When CP was used as the cathode GDL, the performance has deteriorated by a lot. In the case of relatively hydrophilic CP due to no PTFE treatment, it seems that water flooding occurs in the macroporous layer during the activation process and the pores, which are the reactant paths, are clogged and the performance has deteriorated<sup>35, 36</sup>. In contrast, in the case of the CP H, the hydrophobic treatment of the macroporous layer significantly improved performance. PTFE treatment promotes gas transport in the macroporous layer due to the high surface energy at the interface of PTFE and water in the pores, thus ensuring a reactant passage<sup>31, 37, 38</sup>. However, it is still low compared to the performance of AEMFCs using MPL containing GDLs, especially in the current density range where the ohmic overpotential is the dominant loss. Considering that gas is supplied at a high flow rate, carbon papers with relatively large pores have a lower water retention capability in the catalyst layer and tend to dry out the catalyst layer more easily. When CPM L and CPM H were compared, the effect of MPL pore size and hydrophobicity on AEMFC performance was observed. The performance difference was insignificant, but the AEMFC using CPM L as the cathode GDL showed a slightly higher limiting current density. This is because in the case of CPM H, the supply of water to the cathode, which requires

water as a reactant, is slower. Smaller pores and more hydrophobicity properties of CMP H lead to increase in threshold pressure which is the maximum capillary pressure required for water to flow out from the GDLs to catalyst layer.

The optimum performance was obtained when using the GDLs containing the MPL in both the cathode and the anode side. In the case of the anode electrode, the more hydrophobic MPL promotes the back diffusion and the higher performance. Conversely, in the case of the cathode electrode, if the MPL is too hydrophobic, the threshold pressure increases and impedes the supply of water, thereby lowering limiting current density.

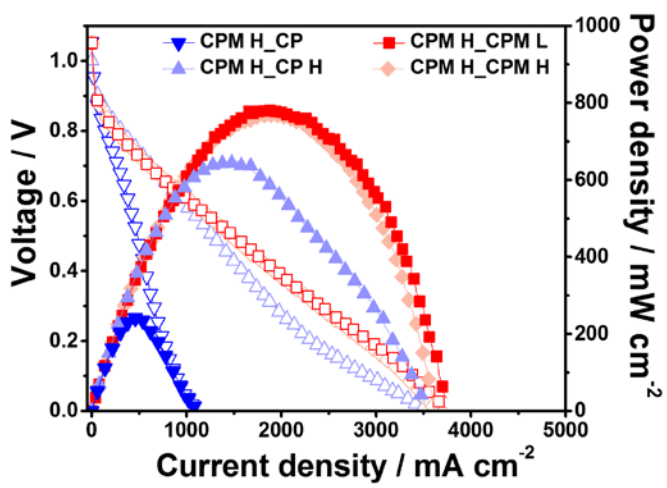


**Figure 2.17** Polarization curves of AEMFC using CP, CP H, CPM L and CPM H as the cathode GDLs and CPM H as the anode GDLs.

## **2.4 Conclusion**

Electrode parameters that are important for performance in AEMFCs using platinum catalyst were investigated. A simple method for enhancing the performance of AEMFCs was described, which was to reduce their ohmic overpotential in the catalyst layer. This was easily achieved by immersing not only the membrane, but the whole MEA in KOH solution before cell operation. The ionic resistance in the catalyst layer decreases to about half of that before KOH treatment, which is confirmed by impedance analysis. The enhancement of cell performance is greater for NPMC (240 %) than for the platinum catalyst (130 %). By accelerating the transfer of water from the anode to the cathode using GDL composed of hydrophobic MPL on carbon paper, it is possible to improve the performance of AEMFCs due to the enhancement of mass transport. Also, the performance is found to depend on the value of the dielectric constant of the solvent of the catalyst ink, which influences the pore structure in the catalyst layer. As the dielectric constant decreases, the catalyst agglomerate size increases due to the increase of the ionomer agglomerate size. This leads to the development of the secondary pores in the catalyst layers. The catalyst layer with well-developed secondary pores has a low ionic resistance due to the advantage of humidified gas transport, thereby improving the performance of AEMFCs.

## 2.5 References

1. R. B. Kaspar, J. A. Wittkopf, M. D. Woodroof, M. J. Armstrong, Y. Yana, *Reverse-Current Decay in Hydroxide Exchange Membrane Fuel Cells*, Journal of the Electrochemical Society, 163, F377-F383, 2016.
2. W. Yang, X. Yue, X. Liu, L. Chen, J. Jia, S. Guo, *Superior Oxygen Reduction Electrocatalysis enabled by Integrating Hierarchical Pores, Fe<sub>3</sub>C Nanoparticles and Bamboo-like Carbon Nanotubes*, Nanoscale 8, 959–964, 2016.
3. Y. J. Sa, D. J. Seo, J. Woo, J. T. Lim, J. Y. Cheon, S. Y. Yang, J. M. Lee, D. Kang, T. J. Shin, H. S. Shin, H. Y. Jeong, C. S. Kim, M. G Kim, T. –Y. Kim, S. H. Joo, *A General Approach to Preferential Formation of Active Fe–N<sub>x</sub> Sites in Fe–N/C Electrocatalysts for Efficient Oxygen Reduction Reaction*, Journal of the American Chemical Society, 138, 15046–15056, 2016.
4. S. Yang, X. Feng, X. Wang, K. Müllen, *Graphene-Based Carbon Nitride Nanosheets as Efficient Metal-Free Electrocatalysts for Oxygen Reduction Reactions*, Angewandte Chemie International Edition, 50, 5339–5343, 2011.
5. C. Chen, X.-D. Yang, Z.-Y. Zhou, Y.-J. Lai, M. Rauf, Y. Wang, J. Pan, L. Zhuang, Q. Wang, Y.-C. Wang, N. Tian, X. –S. Zhang, S. –G Sun, *Aminothiazole-Derived N, S, Fe-Doped Graphene Nanosheets as High Performance Electrocatalysts for Oxygen Reduction*, Chemical Communications, 51, 17092–17095, 2015.
6. E. A. Ticianelli, C. R. Derouin, A. Redondo, S. Srinivasan, *Methods to Advance*

- Technology of Proton Exchange Membrane Fuel Cells*, Journal of the Electrochemical Society, 135, 2209–2214, 1988.
7. R.C. Alkire, H. Gerischer, D. M. Kolb, C. W. Tobias, *Advances in Electrochemical Science and Engineering*, Vol. 5, Wiley-VCH, Weinheim, 1997.
  8. D. Novitski, A. Kosakian, T. Weissbach, M. Secanell, S. Holdcroft, *Electrochemical Reduction of Dissolved Oxygen in Alkaline, Solid Polymer Electrolyte Films*, Journal of the American Chemical Society, 138, 15465–15472, 2016.
  9. H. Zhang, H. Ohashi, T. Tamaki, T. Yamaguchi, *Water Movement in a Solid-State Alkaline Fuel Cell Affected by the Anion-Exchange Pore-Filling Membrane Properties*, The Journal of Physical Chemistry C, 117, 16791-16801, 2013.
  10. J. R. Varcoe, P. Atanassov, D. R. Dekel, A. M. Herring, M. A. Hickner, P. A. Kohl, A. R. Kucemak, W. E. Mustain, K. Nijmeijer, K. Scott, T. Xu, L. Zhuang, *Anion-exchange membranes in electrochemical energy systems*. Energy & Environmental Science, 7, 3135–3191, 2014.
  11. D. M. Bernardi, M. W. Verbrugge, *A Mathematical Model of the Solid-Polymer-Electrolyte Fuel Cell*, Journal of the Electrochemical Society, 139, 2477–2491, 1992.
  12. Y. Tang, J. Zhang, C. Song, H. Liu, J. Zhang, J. Zhang, H. Wang, S. Mackinnon, T. Peckham, J. Li, S. McDermid, P. Kozak, *Temperature Dependent*

*Performance and In Situ AC Impedance of High-Temperature PEM Fuel Cells Using the Nafion-112 Membrane*, Journal of the Electrochemical Society, 153, A2036-A2043, 2006.

13. A. Filpia, M. Bocciaa, H.A. Gasteiger, *Pt-Free Cathode Catalyst Performance in H<sub>2</sub>/O<sub>2</sub> Anion-Exchange Membrane Fuel Cells (AMFCs)*, ECS Transactions, 16, 1835–1845, 2008.
14. M. Tanaka, M. Koike, K. Miyatake, M. Watanabe, *Synthesis and Properties of Anion Conductive Ionomers Containing Fluorenyl Groups for Alkaline Fuel Cell Applications*, Polymer Chemistry, 2, 99-106, 2011.
15. T. D. Myles, K. N. Grew, A. A. Peracchio, W. K. S. Chiu, *Transient ion exchange of anion exchange membranes exposed to carbon dioxide*, Journal of Power Sources, 296, 225-236, 2015.
16. P. M. Gomadam, J. W. Weidner, *Analysis of Electrochemical Impedance Spectroscopy in Proton Exchange Membrane Fuel Cells*, International Journal of Energy Research, 29, 1133–1151, 2005.
17. R. Makharia, M.F. Mathias, D.R. Baker, *Measurement of Catalyst Layer Electrolyte Resistance in PEFCs Using Electrochemical Impedance Spectroscopy*, Journal of the Electrochemical Society, 152, A970–A977, 2005.
18. J. H. Jang, S. Jeon, J. H. Cho, S. -K. Kim, S. -Y. Lee, E. A. Cho, H. -J. Kim, J. Han, T. -H. Lim, *Complex Capacitance Analysis of Ionic Resistance and*

- Interfacial Capacitance in PEMFC and DMFC Catalyst Layers*, Journal of the Electrochemical Society, 156, B1293–B1300, 2009.
19. J. H. Jang, S. M. Oh, *Complex Capacitance Analysis of Impedance Data and its Applications*, Journal of the Korean Electrochemical Society, 13, 223–234, 2010.
20. X. -Z. R. Yuan, C. Song, H. Wang, J. Zhang, *Electrochemical Impedance Spectroscopy in PEM Fuel Cells: Fundamentals and Applications*, Springer-Verlag, London, 2010.
21. O.-H. Kim, Y.-H. Cho, D.Y. Chung, M. J. Kim, J. M. Yoo, J. E. Park, H. Choe, Y.-E. Sung, *Facile and Gram-scale Synthesis of Metal-free Catalysts: Toward Realistic Applications for Fuel Cells*, Scientific Reports, 5, 8376, 2015.
22. G Gebel, B. Loppinet, *Colloidal structure of ionomer solutions in polar solvents*, *Journal of Molecular Structure*, 383, 43-49, 1996.
23. Y. S. Kim, C. F. Welch, N. H. Mack, R. P. Hjelm, E. B. Orler, M. E. Hawley, K. S. Lee, S.-D. Yim, C. M. Johnston, *Highly durable fuel cell electrodes based on ionomers dispersed in glycerol*, *Physical Chemistry Chemical Physics*, 16, 5927-5932, 2014.
24. T. T. Ngo, T. L. Yu, H. -L. Lin, Influence of the composition of isopropyl alcohol/water mixture solvents in catalyst ink solutions on proton exchange membrane fuel cell performance, *Journal of Power Sources*, 225, 293-303, 2013.
25. Y.G Yoon, GG Park, T.H. Yang, J.N. Han, W.Y. Lee, C.S. Kim, *Effect of pore*

- structure of catalyst layer in a PEMFC on its performance*, International Journal of Hydrogen Energy, 28, 657–662, 2003.
26. E. Passalacqua, F. Lufrano, G. Squadrato, A. Patti, L. Giorgi, *Influence of the structure in low-Pt loading electrodes for polymer electrolyte fuel cells*, Electrochimica Acta, 43, 3665–3673, 1998.
27. R. O’Hayre, S. Cha, W. Colella, F. B. Prinz, Fuel cell fundamentals, John Wiley & Sons, 2009.
28. Q. Yan, H. Toghiani, J. Wu, *Investigation of water transport through membrane in a PEM fuel cell by water balance experiments*, Journal of Power Sources, 158, 316-325, 2006.
29. K. H. Choi, D. H. Peck, C. S. Kim, D. R. Shin, T. H. Lee, *Water transport in polymer membranes for PEMFC*, Journal of Power Sources, 86, 197-201, 2000.
30. H Zhang, H. Ohashi, T. Tamaki, T. Yamaguchi, *Water Movement in a Solid-State Alkaline Fuel Cell Affected by the Anion-Exchange Pore-Filling Membrane Properties*, The Journal of Physical Chemistry C, 177, 16791-16801, 2013.
31. S. Park, J. W. Lee, B. N. Popov, *A review of gas diffusion layer in PEM fuel cells: Materials and designs*, International Journal of Hydrogen Energy, 37, 5850-5865, 2012.
32. J. T. Gostick, M. A. Ioannidis, M. W. Fowler, M. D. Pritzker, *On the role of the microporous layer in PEMFC operation*, Electrochemistry Communications, 11,

- 576-579, 2009.
33. A. Z. Weber, J. Newman, *Effects of Microporous Layers in Polymer Electrolyte Fuel Cells*, Journal of The Electrochemical Society, 152, A677-A688, 2005.
34. U. Pasaogullari, C. -Y. Wang, *Two-phase transport and the role of micro-porous layer in polymer electrolyte fuel cells*, Electrochimica Acta, 49, 4359-4369, 2004.
35. G -G Park, Y. -J. Sohn, T. -H. Yang, Y. -G Yoon, W. -Y. Lee, C. -S. Kim, *Effect of PTFE contents in the gas diffusion media on the performance of PEMFC*, Journal of Power Sources, 131, 182-187, 2004.
36. S. Shimpalee, U. Beuscher, J. W. Van Zee, *Analysis of GDL flooding effects on PEMFC performance*, Electrochimica Acta, 52, 6748-6754, 2007.
37. A. D. Santamaria, P. K. Das, J. C. MacDonald, A. Z. Weber, *Liquid-Water Interactions with Gas-Diffusion-Layer Surfaces*, Journal of the Electrochemical Society, 161, F1184-F1193, 2014.
38. J. Benziger, J. Nehlsen, D. Blackwell, T. Brennan, J. Itescu, *Water flow in the gas diffusion layer of PEM fuel cells*, Journal of Membrane Science, 261, 98-106, 2005.

## **Chapter 3 Strategies for Improving the Performance of AEMFCs with Non Precious Metal Cathode Catalysts**

### **3.1 Introduction**

Electrocatalysts for the oxygen reduction and evolution reactions have been considered crucial in the electrochemistry field for the development of sustainable energy storage and conversion devices such as the metal-air battery, water splitting and fuel cells<sup>1-4</sup>. Oxygen reduction electrocatalysts are especially important in polymer electrolyte membrane fuel cells (PEMFCs), since oxygen reduction reaction (ORR) catalysts are the key component in determining performance and cost<sup>5</sup>. The usage of highly active and inexpensive ORR catalyst is vital for the extensive introduction of fuel cell-powered systems. Platinum (Pt) has the highest catalytic activity and is the most widespread catalyst for ORR in acidic and basic electrolytes. However, the high cost of Pt is one of the barriers to furthering the commercialization of fuel cell application. Since the cost of the catalyst layer is responsible for around 46% of material costs for the fuel cell stack<sup>5</sup>, many groups have focused on reducing Pt loading to reduce the costs by controlling surface structure and composition of the Pt based catalyst (Pt alloy, core shell structure and nanostructured thin film)<sup>6-9</sup>. However, the scarcity and low CO tolerance of Pt lead

to many attempts to develop Pt-free catalysts<sup>10</sup>. Therefore, considerable efforts have been made towards the development of non-precious metals catalysts (NPMCs)

Carbon based catalysts have been studied extensively among NPMCs, particularly transition metals and N doped carbon (TM-N-C) catalysts<sup>11-13</sup>. These are considered the most promising candidates because of their high ORR activity and CO tolerance with inexpensive materials<sup>14</sup>. Several TM-N-C catalysts have reported excellent ORR activity comparable to Pt. But their superior performance is limited only to the results in half-cell applications. In most of those papers, the loading of the synthesized catalyst used for the half-cell test was 5 to 80 times higher than that of Pt (Figure 3.1)<sup>15-19</sup>. It is generally known that carbon-based catalysts have improved performance as catalyst loading increases in the half-cell test<sup>20-21</sup>. Therefore, to achieve performance trends similar to that of half-cell performance in a single cell, performance measurements should be performed on the single cell using the same amount of catalyst loading difference as used in the half cell test; i.e. synthesized catalysts should be deposited 5 to 80 times higher than Pt. However, when the application of catalysts was converted from the half-cell to the single-cell, several electrode conditions have changed such as the use of solid electrolyte, mass transport of reactants and products and conduction of ion and electron. Accordingly, when the thickness of the electrode is increased as the loading amount of the catalyst is increased, ohmic and mass transport have become

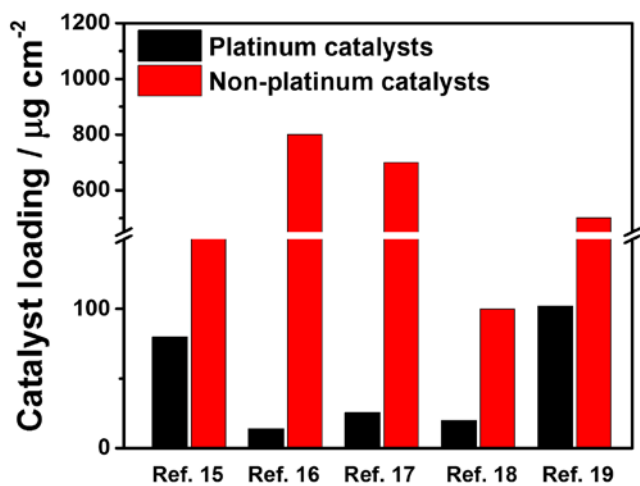


**Figure 3.1** Reported catalysts loading of NPMCs compared to Pt catalyst in the half-cell system in several papers.

major factors for reducing the performance of the single-cell. One of the strategies that can improve these loss factors is to increase the active site density to reduce the amount of catalyst loading. However, an effective method from the viewpoint of membrane-electrode assembly (MEA) is to reduce the diffusion length of reactants or developing secondary pores to facilitate the transport of reactants and products in the catalyst layer even if the amount of catalyst loading is high. In this chapter, overcoming the challenges with different trends of performance between in single-cell and half-cell systems will be discussed with respect to electrode engineering to decrease the transport resistance.

## **3.2 Experimental**

### **3.2.1 Materials Preparation**

#### **Synthesis of CS-FeN-C<sup>22</sup>**

Ferrous phthalocyanine and 9,9'-Bianthracene, 10,10'-dibromo monomer were dispersed in hexane solution. After complete dispersion, NaCl was added to the solution as a template and dried overnight at 70 °C with stirring. The solvent was evaporated and heat treated at 200 °C and 450 °C sequentially. NaCl template was simply removed by washing the mixture several times with deionized (DI) water.

#### **Synthesis of LP\_FeN-C and SP\_FeN-C<sup>23</sup>**

Pluronic F127 was dissolved in the ethanol and 0.2 M HCl. Iron (II) chloride tetrahydrate and 1,10-phenanthroline were mixed in the ethanol and 0.2 M HCl to form Fe(phen)<sub>3</sub>Cl<sub>2</sub> complex. Resol, tetraethylorthosilicate (TEOS) and the Fe(phen)<sub>3</sub>Cl<sub>2</sub> complex solution were added to the polymer solution. After stirred the mixed solution, the solvent was evaporated and dried overnight at 100 °C and heat treated at 900 °C. Silica in the framework was removed by etching in diluted HF solution. Subsequently, secondary heat treatment was carried out in Ar at 900 °C to obtain a FeN-C catalyst having a large particle size (LP\_FeN-C). For reference, the smaller particle sized FeN-C catalyst (SP\_FeN-C) was synthesized using the same precursors as in LP\_FeN-C synthesis.

### **Preparation of MEAs**

The catalyst inks were prepared by sonicating a mixture of synthesized catalysts, solvents, commercial ionomer and DI water. After the catalyst inks completely homogenized, it was sprayed onto the commercial membrane (A901, Tokuyama). The active electrode area was 5 cm<sup>2</sup>. The cathode catalyst loading of Pt/C 40 wt% (Johnson Matthey Co.) and the synthesized catalysts were 1mg cm<sup>-2</sup>. The anode catalyst was deposited Pt/C 40 wt% (Johnson Matthey Co.) with 0.5 mg cm<sup>-2</sup> for all the MEAs. The catalyst coated membranes (CCMs) were dried overnight in the air. And the CCMs immersed in 1 M KOH solution for an hour and rinsed with DI water several times before the single-cell assembly. Gas diffusion layers (35BC, SGL) were placed at the side of CCMs.

### **3.2.2 Characterizations and Electrochemical Test**

#### **Characterization techniques**

The field-emission scanning electron microscopy (FE-SEM, MERLIN Compact, ZEISS) and the transmission electron microscopy (TEM, Technai F20, FEI and JEM 2010, JEOL) were used to confirm the morphology of the electrodes and catalysts. The secondary pore size of electrodes was obtained using Mercury porosimetry (Micro Active AutoPore V 9600, Micromeritics).

### **Electrochemical analysis**

The half-cell test was carried out in a three-electrode system using a potentiostate (Eco Chemie). This consisted of a glassy carbon electrode coated with a catalyst as working electrode, a Pt wire as a counter electrode, and an Ag / AgCl electrode as a reference electrode. The catalyst inks were prepared by sonicating a mixture of catalyst, solvent, Nafion® ionomer. And the catalyst inks were deposited onto the ring disk electrode (RDE) ( $0.196\text{ cm}^2$ , PINE). The measurement was conducted with a scan rate of  $5\text{ mV s}^{-1}$  in  $\text{O}_2$ -saturated  $0.1\text{ M KOH}$  solution of  $20\text{ }^\circ\text{C}$ . The rotation speed of RDE was 1600 rpm. For the reference, Pt/C 20 wt% (Johnson Matthey Co.) was used. Polarization curves of AEMFCs were measured using the fuel cell test system (CNL energy Co.). Before measuring the polarization curves, a single-cell was operated at a constant voltage of  $0.1\text{ V}$  for decarbonation within a CCMs. Humidified hydrogen was supplied to the anode and humidified oxygen or air was supplied to the cathode. Polarization curves were measured using a current-sweep method with increasing current at a rate of  $10\text{ mA cm}^{-2}\text{ s}^{-1}$  until the cell voltage reaches  $0.3\text{ V}$ . The cell temperature was maintained at  $50\text{ }^\circ\text{C}$ . While operating fuel cells, the total outlet pressures were 1.8 bar.

### **3.3 Results and Discussion**

#### **3.3.1 Applying Carbon Sheet Structure to Cathode Catalyst for High Volumetric Performance of AEMFC**

Most papers that apply NPMCs as a cathode catalyst in a single-cell have a catalyst loading of NPMCS that is 5 to 20 times higher than the typical loading of commercial platinum catalyst used in a PEMFC<sup>24-26</sup>, which can cause severe volume problems when applied to a stack. Accordingly, when the US department of energy (DOE) evaluates the performance of NPMCS, it is based on the volume normalized performance<sup>27</sup>. The application of the carbon sheet structure can be a method suitable for the requirements of DOE. It is expected to reduce the diffusion length of reactants and products inside the MEAs, and thereby reducing the ohmic and mass transfer overpotential. This consequently improves the performance of AEMFCs. The synthesis process of the Fe-N doped carbon sheet catalyst is described in the Figure 3.2. Ferrous phthalocyanine and 9,9'-Bianthracene, 10,10'-dibromo monomer used as N-coordinated Fe and carbon nanoribbon precursor, respectively<sup>22</sup>. NaCl was used as a flat template. Figure 3.3 shows a Fe-N doped carbon sheet (CS-FeN-C) formed on a flat surface of NaCl. After the NaCl template was removed, CS-FeN-C structure was obtained. The synthesized CS-FeN-C has a two dimensional and thin structure

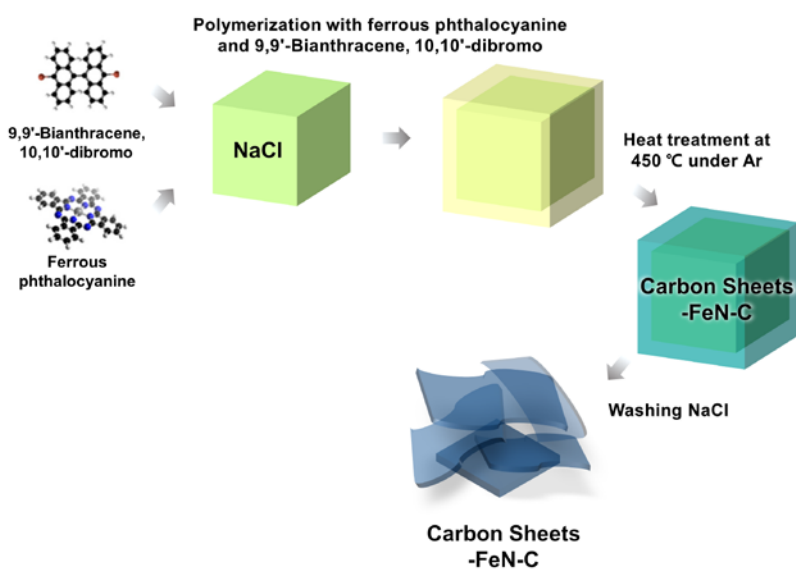


**Figure 3.2** Schematic illustration of synthesis of CS-FeN-C.

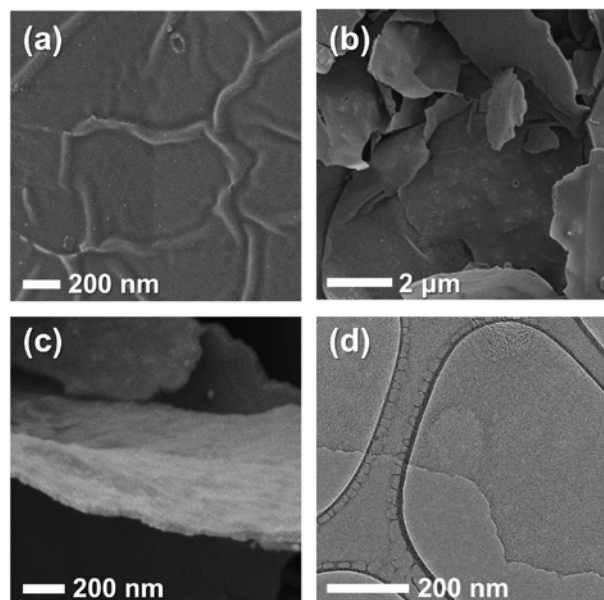


**Figure 3.3** FE-SEM images of CS-FeN-C (a) before, (b) after removal of NaCl and (c) its enlarged image. (d) TEM image of CS-FeN-C.

as seen in scanning electron microscopy (SEM) and transmission microscopy (TEM) images (Figure 3.3). The thickness of synthesized catalyst is confirmed to be about 20 nm through an enlarged SEM image. In order to confirm the advantages of the carbon sheet structure in the practical operation, the synthesized catalyst was applied to a single-cell. The performance of CS-FeN-C was compared with that of Fe-N doped carbon supported on carbon black, which is commonly used as a support material. When the catalyst loading of both catalysts were identical as  $1 \text{ mg cm}^{-2}$ , the thickness of CS-FeN-C catalyst layer is  $28.7 \pm 0.3 \mu\text{m}$ , which is 19 % thinner than that of carbon supported CB-FeN-C catalyst layer ( $35.2 \pm 0.4 \mu\text{m}$ ) (Figure 3.4 (a) and (b)). The single-cell performance of AEMFC with CS-FeN-C and CB-FeN-C are shown in Figure 3.4 (c). The polarization and power density curves of CS-FeN-C exhibit higher than that of CB-FeN-C when the performance is normalized by volume of cathode catalyst layer. The maximum power densities of CS-FeN-C and CB-FeN-C are  $63 \text{ W cm}^{-3}$  and  $36 \text{ W cm}^{-3}$ , respectively. The performance of CS-FeN-C was also compared to that of commercial Pt/C 40 wt% in the single-cell. The thickness of CS-FeN-C catalyst layer is 24.9 % thinner than that of commercial Pt/C 40 wt% when the same amount of catalyst is loaded ( $1 \text{ mg cm}^{-2}$ ) (Figure 3.5). The performance of CS-FeN-C is comparable to that of Pt/C 40 wt% in the half-cell test (Figure 3.6 (a)). However, AEMFC with CS-FeN-C

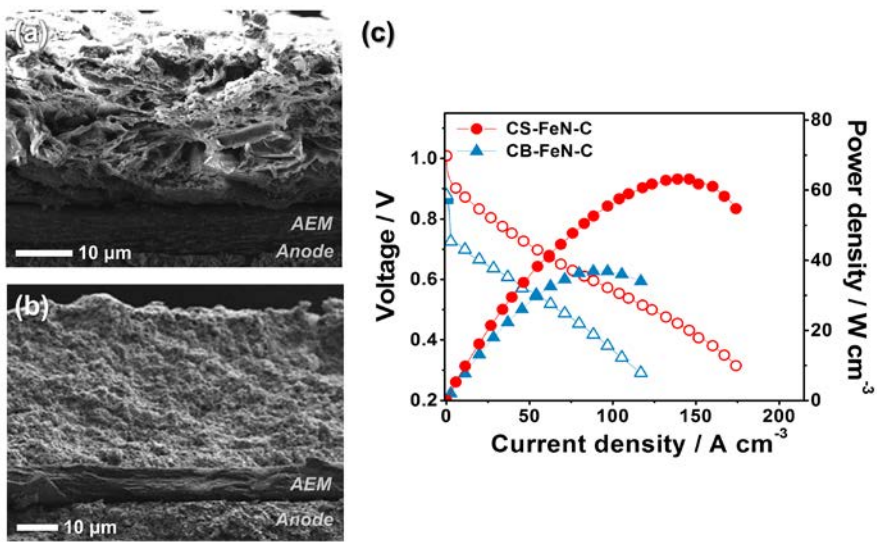


**Figure 3.4** FE-SEM cross sectional images of MEA with (a) CS-FeN-C and (b) CB-FeN-C. (c) Polarization ( $\circ$ ,  $\Delta$ ) and power density ( $\bullet$ ,  $\blacktriangle$ ) curves of AEMFCs using CS- and CB-FeN-C (normalized by volume of cathode catalyst layer).

shows a higher performance than that using Pt/C 40 wt% in the low current density range where the performance loss mainly caused by mass transport in the catalyst layer (Figure 3.6 (b)). The maximum power density of CS-FeN-C is 35 % higher than that of Pt/C 40 wt% ( $53 \text{ W cm}^{-3}$ ). This indicates that the thin electrode thickness of carbon sheet structure achieves the benefits of mass transfer and ionic conduction and improved performance of AEMFC, as it reduces the diffusion length.

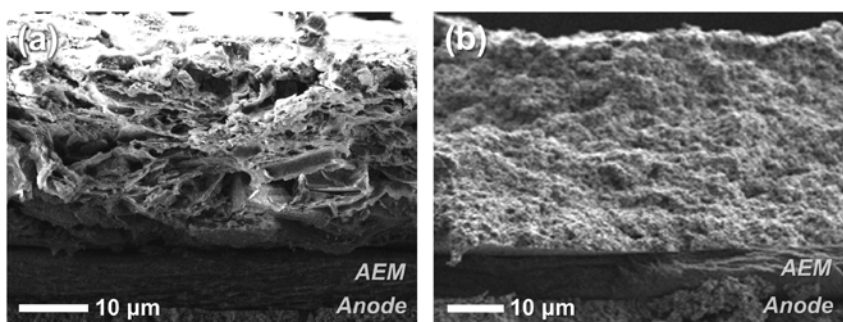


**Figure 3.5** FE-SEM cross sectional images of MEA with (a) CS-FeN-C and (b) Pt/C 40 wt%.

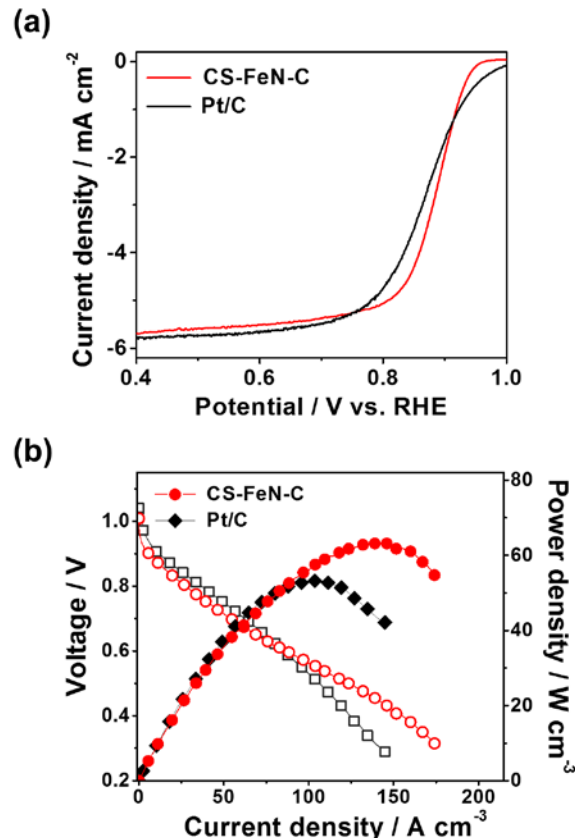


**Figure 3.6** (a) ORR polarization curves of CS-FeN-C and Pt/C. (b) Polarization ( $\circ$ ,  $\Delta$ ) and power density ( $\bullet$ ,  $\blacktriangle$ ) curves of CS-FeN-C and Pt/C normalized by volume of cathode catalyst layer.

### **3.3.2 Tailoring the Secondary Pore Structure in the Cathode Catalyst Layer for Improving the Mass Transfer**

In order to confirm the relationship between the secondary pore structure and the performance of AEMFC with NPMC as a cathode catalyst, catalysts of different particle sizes were synthesized using the same precursor. Figure 3.7 shows the morphology of synthesized Fe, N doped carbon catalysts with a large particle size (LP\_FeN-C) and a small particle size (SP\_FeN-C). To compensate for the active surface area when using the large diameters catalysts, the catalysts are composed of a mesoporous structure as can been seen in the Figure 3.7 (c), (d). The ORR activities of catalysts were assessed in half-cell system in 0.1 M KOH solution. As shown in Figure 3.8 (a), the ORR activity of LP\_FeN-C is comparable to that of SP\_FeN-C. It can be deduced from the results that the difference in performance in a single-cell is due to the MEA factors, not the difference in catalytic activity between the two catalysts.

The effect of the difference in particle sizes on the performance of AEMFCs was investigated in a single-cell (Figure 3.8 (b)). Catalyst loading on the cathode side is the same for both LP\_FeN-C and SP\_FeN-C as  $1 \text{ mg cm}^{-2}$ . The polarization curve of MEA with LP\_FeN-C is similar to that of MEA with SP\_FeN-C in the low current density region where the voltage loss is dominated

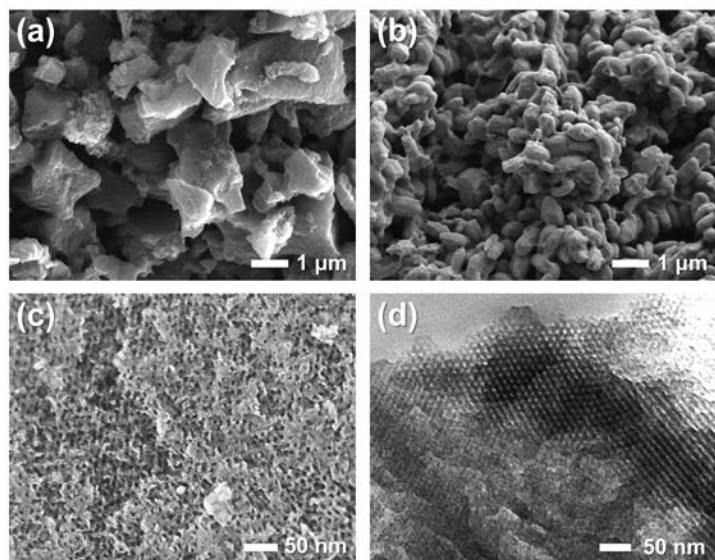


**Figure 3.7** FE-SEM images of (a) LP\_FeN-C and (b) SP\_FeN-N. Magnified (c) SEM and (d) TEM images.

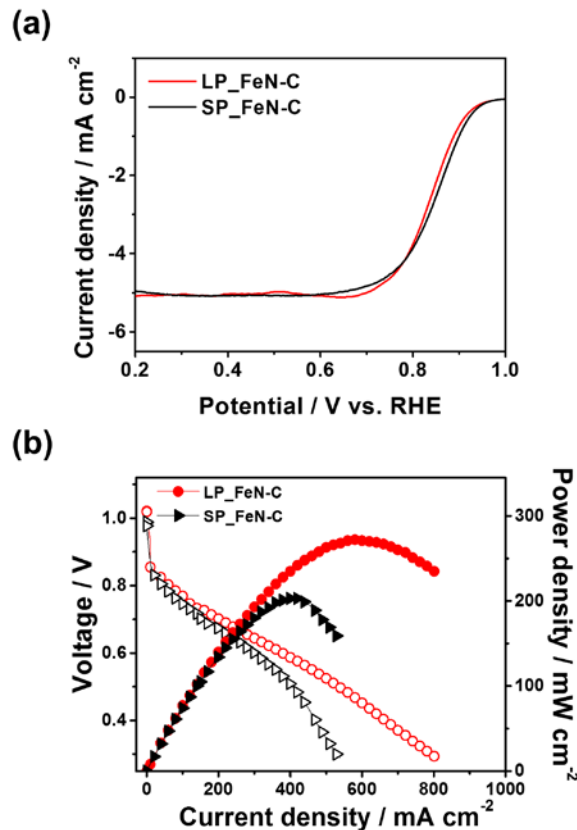


**Figure 3.8** (a) ORR polarization curves of LP\_FeN-C and SP\_FeN-C. (b) Polarization ( $\circ$ ,  $\Delta$ ) and power density ( $\bullet$ ,  $\blacktriangle$ ) curves of LP\_FeN-C and SP\_FeN-C.

by the activation overpotential. However, LP\_FeN-N showed higher performance than SP\_FeN-C when the voltage is lower than 0.7 V where the low performance is attributed to the higher ohmic and mass transfer resistance. The current densities of AEMFC with LP\_FeN-C and SP\_FeN-C are 380 mA cm<sup>-2</sup> and 289 mA cm<sup>-2</sup> at 0.6 V and 662 mA cm<sup>-2</sup> and 269 mA cm<sup>-2</sup> at 0.4 V. This is because the particle size of LP\_FeN-C is larger than that of SP\_FeN-C, the secondary pores, which are the space between the particles, are well developed in the catalyst layer composed of LP\_FeN-C catalysts as seen in the cross sectional SEM images of the electrodes (Figure 3.9). Further analysis of secondary pore sizes were carried out using the mercury intrusion porosimetry. The pore size distributions (Figure 3.10 (a)) are clearly showed larger and further developed the secondary pores in LP\_FeN-C electrode. Well-developed secondary pores in the catalyst layer of LP\_FeN-C promotes the transfer of reactants and products, and thus easily leads to even distribution of water through the catalyst layer. This reduces the mass transfer resistance and the ohmic resistance, which is mainly dependent on the hydration state of the ionomer. As the average secondary pore size increases from 200 nm to 670 nm, oxygen utilization increases by 49 % and maximum power density is improved from 200 mW cm<sup>-2</sup> to 272 mW cm<sup>-2</sup> (Figure 3.10 (b)).

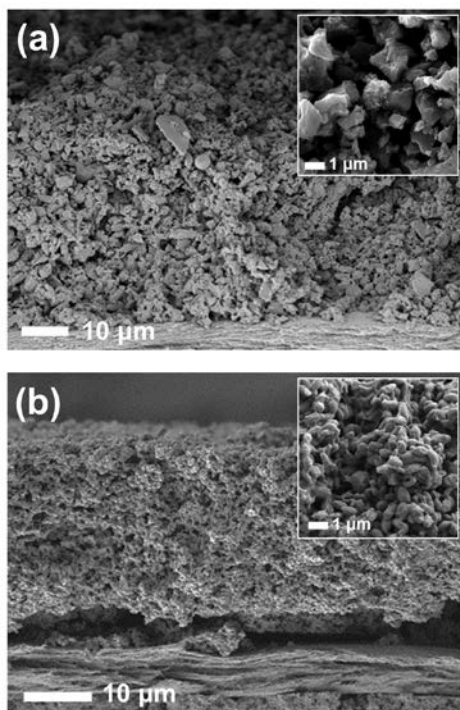


**Figure 3.9** FE-SEM cross sectional images of MEA with (a) LP\_FeN-C and (b) SP\_FeN-C cathodes.

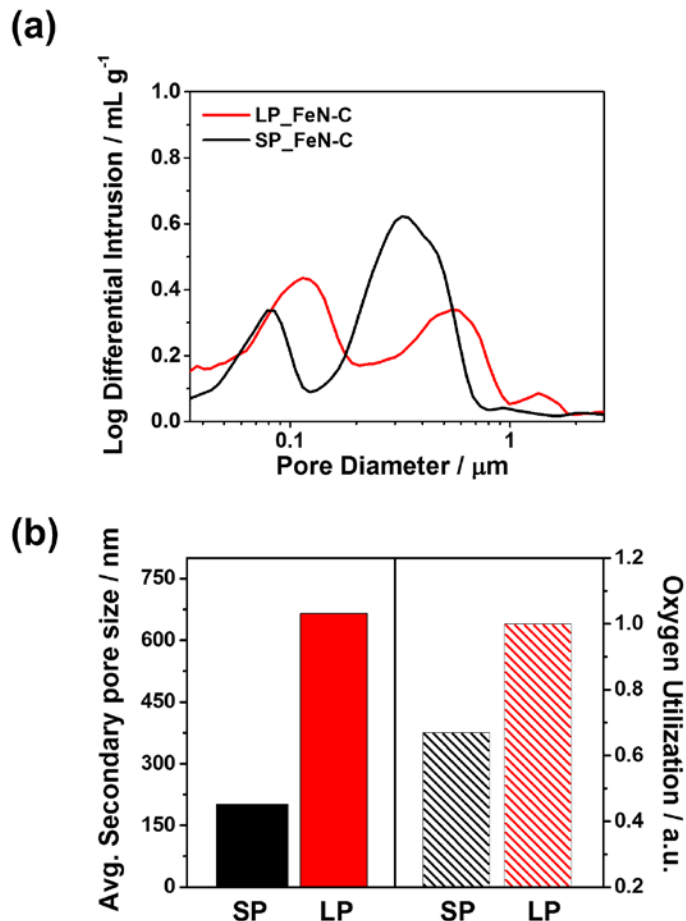


**Figure 3.10** (a) Pore size distribution of LP\_FeN-C and SP\_FeN-C cathodes. (b) Changes in average secondary pore size and oxygen utilization in LP\_FeN-C and SP\_FeN-C cathodes.

The performance of LP\_FeN-C in a single-cell has compared to the performance when using commercial Pt/C catalysts (Figure 3.11). The catalyst loading of Pt/C is the same as LP\_FeN-C at  $1 \text{ mg cm}^{-2}$ . Figure 3.12 shows the cross sectional SEM images of LP\_FeN-C and Pt/C cathode. The difference in pore structure between two catalysts was clearly observed even at low magnification of SEM images. This difference also can be supported by the pore size distribution curves of electrode using LP\_FeN-C and Pt/C. It has demonstrated that the secondary pore structure in the LP\_FeN-C cathode is better developed than in the Pt/C cathode as shown in Figure 3.13 (a). The current density of AEMFC with LP\_FeN-C exhibits  $801 \text{ mA cm}^{-2}$  which is 37 % higher than the current density of the AEMFC with the Pt/C electrode at  $0.3 \text{ V}$  where the mass transfer dominant region. The superior mass transfer characteristic was further corroborated by oxygen gain analysis. The oxygen gain is general indicator of performance loss originating from the mass transport. This value can be obtained by calculating the difference in voltage when oxygen and air are fed into the cathode as a function of current densities. As seen in Figure 3.13 (b), AEMFC with the LP\_FeN-C cathode shows much lower oxygen gain compared to that with the Pt/C cathode. This demonstrates that AEMFC with a LP\_FeN-C cathode has electrode properties favorable for mass transfer than AEMFC with a Pt/C cathode. Therefore when electrode

thickness and catalyst loadings are comparable, AEMFC with LP\_FeN-C exhibits a higher power density than that with Pt/C, due to the enhancement of ohmic and mass transport in the catalyst layer.

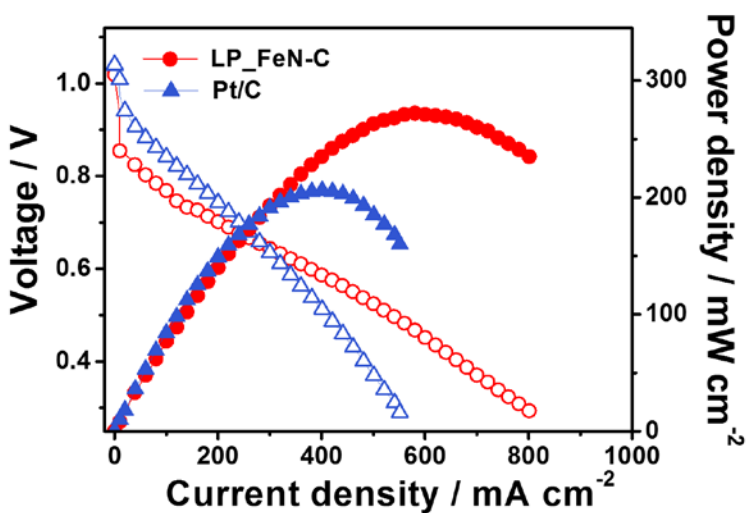


**Figure 3.11** Polarization ( $\circ$ ,  $\Delta$ ) and power density ( $\bullet$ ,  $\blacktriangle$ ) curves of AEMFCs with LP\_FeN-C and Pt/C cathodes.

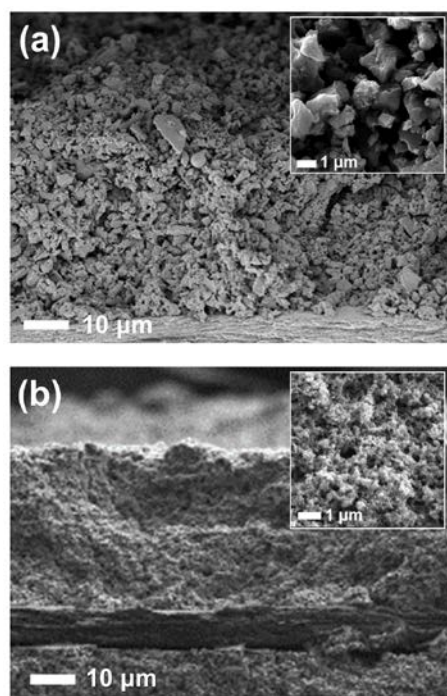
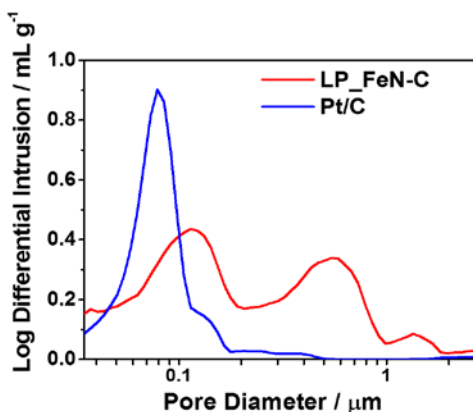


**Figure 3.12** FE-SEM cross sectional images of MEA with (a) LP\_FeN-C and (b) Pt/C cathodes.

(a)



(b)

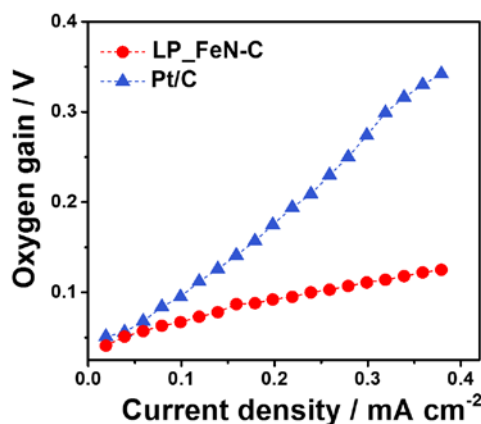


**Figure 3.13** (a) Pore size distribution of LP\_FeN-C and Pt/C cathodes. (b) Oxygen gain as a function of current density for AEMFCs with LP\_FeN-C and Pt/C cathodes.

### **3.4 Conclusion**

The iron and nitrogen doped carbon-based catalyst were designed in consideration of the important electrode parameters in the single-cell performance. This is revealed in the previous chapter and their impact on the performance of AEMFCs is analyzed. The main factors that degrade the performance of NPMC in a single-cell are the ohmic and mass transfer resistances due to the thick electrodes. These are not major factors affecting half-cell performance.

To reduce ohmic and mass transport losses, a catalyst with a carbon sheet structure for reducing diffusion length has been proposed first. When CS-FeN-C catalyst having a carbon sheet structure used for the cathode of AEMFC, the electrode thickness could be reduced by 20 %, from 35.2  $\mu\text{m}$  to 28  $\mu\text{m}$  compared to when CB-FeN-C is deposited on the common carbon support material. AEMFC with CS-FeN-C cathode achieves higher volumetric performance than AEMFC with Pt/C cathode. Finally, a catalyst having a large particle size for easy generation of secondary pores is suggested. The oxygen utilization rate of AEMFC with LP\_FeN-C has improved by 49 % compared to AEMFC with SP\_FeN-C because of its advantageous structure for mass transport. When LP\_FeN-C and Pt/C cathodes have a comparable thickness

and catalyst loading, the AEMFC with the LP\_FeN-C cathode exhibits a higher power density than that with the Pt/C, due to the enhancement of ohmic and mass transport in the catalyst layer.

## 2.5 References

1. R. B. Kaspar, J. A. Wittkopf, M. D. Woodroof, M. J. Armstrong, Y. Yana, *Reverse-Current Decay in Hydroxide Exchange Membrane Fuel Cells*, Journal of the Electrochemical Society, 163, F377-F383, 2016.
2. W. Yang, X. Yue, X. Liu, L. Chen, J. Jia, S. Guo, *Superior Oxygen Reduction Electrocatalysis enabled by Integrating Hierarchical Pores, Fe<sub>3</sub>C Nanoparticles and Bamboo-like Carbon Nanotubes*, Nanoscale 8, 959–964, 2016.
3. B. Y. Xia, Y. Yan, N. Li, H. B. Wu, X. W. D. Lou, X. Wang, *A metal–organic framework-derived bifunctional oxygen electrocatalysts*, Nature Energy, 1, 15006, 2016.
4. C. C. L. McCrory, S. Jung, I. M. Ferrer, S. M. Chatman, J. C. Peters, T. F. Jaramilo, *Benchmarking hydrogen evolving reaction and oxygen evolving reaction electrocatalysts for solar water splitting devices*, Journal of the American Chemical Society, 137, 4347–4357, 2015.
5. U.S. Department of Energy Hydrogen and Fuel Cells Program 2017, [https://www.Hydrogen.energy.gov/pdfs/review17/2017\\_amr\\_07\\_manufacturing\\_rd.pdf](https://www.Hydrogen.energy.gov/pdfs/review17/2017_amr_07_manufacturing_rd.pdf)
6. D. Wang, H. L. Xin, R. Hovden, H. Wang, Y. Yu, D. A. Muller, F. J. DiSalvo, H.

- D. Abruña, *Structurally ordered intermetallic platinum–cobalt core–shell nanoparticles with enhanced activity and stability as oxygen reduction electrocatalysts*, Nature Materials, 12, 81–87, 2013.
7. K. Gong, D. Su, R. R. Adzic, *Platinum-monolayer shell on AuNi<sub>0.5</sub>Fe nanoparticle core electrocatalyst with high activity and stability for the oxygen reduction reaction*, Journal of the American Chemical Society, 132, 14364–14366, 2010.
8. J. Erlebacher, J. Snyder, *Dealloyed nanoporous metals for PEM fuel cell catalysis*, ECS Transactions, 25, 603–612, 2009.
9. B. Lim, M. Jiang, P. H. C. Camargo, E. C. Cho, J. Tao, X. Lu, Y. Zhu, Y. Xia, *Pd-Pt bimetallic nanodendrites with high activity for oxygen reduction*, Science, 324, 1302–1305, 2009.
10. Z. -C. Zhang, X. -C. Tian, B. -W. Zhang, L. Huang, F. -C. Zhu, X. -M. Qu, L. Liu, S. Liu, Y. -X. Jiang, S. -G. Sun, *Engineering phase and surface composition of Pt<sub>3</sub>Co nanocatalysts: A strategy for enhancing CO tolerance*, Nano Energy, 34, 224–232, 2017.
11. Y. Yao, Y. You, G. Zhang, J. Liu, H. Sun, Z. Zou, S. Sun, *Highly Functional Bioinspired Fe/N/C Oxygen Reduction Reaction Catalysts: Structure-Regulating Oxygen Sorption*, ACS applied materials & interfaces, 8, 6464–6471, 2016.
12. A. Serov, K. Artyushkova, P. Atanassov, *Fe-N-C Oxygen Reduction Fuel Cell*

*Catalyst Derived from Carbendazim: Synthesis, Structure, and Reactivity*, Advanced Energy Materials, 4, 1301735, 2014.

13. C. Zhu, H. Li, S. Fu, D. Du, Y. Lin, *Highly efficient nonprecious metal catalysts towards oxygen reduction reaction based on three-dimensional porous carbon nanostructures*, Chemical Society Reviews, 45, 517–531, 2016.
14. W. Niu, L. Li, X. Liu, N. Wang, J. Liu, W. Zhou, Z. Tang, S. Chen, *Mesoporous N-Doped Carbons Prepared with Thermally Removable Nanoparticle Templates: An Efficient Electrocatalyst for Oxygen Reduction Reaction*, Journal of the American Chemical Society, 137, 5555–5562, 2015.
15. H. Ren, Y. Wang, Y. Yang, X. Tang, Y. Peng, H. Peng, L. Xiao, J. Lu, H. D. Abruña, L. Zhuang, *Fe/N/C Nanotubes with Atomic Fe Sites: A Highly Active Cathode Catalyst for Alkaline Polymer Electrolyte Fuel Cells*, ACS Catalysis, 7, 6485-6492, 2017.
16. Y. J. Sa, D. J. Seo, J. Woo, J. T. Lim, J. Y. Cheon, S. Y. Yang, J. M. Lee, D. Kang, T. J. Shin, H. S. Shin, H. Y. Jeong, C. S. Kim, M. G Kim, T. –Y. Kim, S. H. Joo, *A General Approach to Preferential Formation of Active Fe–N<sub>x</sub> Sites in Fe–N/C Electrocatalysts for Efficient Oxygen Reduction Reaction*, Journal of the American Chemical Society, 138, 15046-15056, 2016.
17. W. J. Jiang, L. Gu, L. Li, Y. Zhang, X. Zhang, L.-J. Zhang, J. -Q. Wang, J. -S. Hu,

- Z. Wei, L. -J. Wan, *Understanding the High Activity of Fe–N–C Electrocatalysts in Oxygen Reduction: Fe/Fe<sub>3</sub>C Nanoparticles Boost the Activity of Fe–N<sub>x</sub>*, Journal of American Chemical Society, 138, 3570-3578, 2016.
18. L. Lin, Q. Zhu, A. W. Xu, *Noble-metal-free Fe–N/C catalyst for highly efficient oxygen reduction reaction under both alkaline and acidic conditions*, Journal of the American Chemical Society, 136, 11027-11033, 2014.
19. Y. Han, Y. G Wang, W. Chen, R. Xu, L. Zheng, J. Zhang, J. Luo, R. -A. Shen, Y. Zhu, W.-C. Cheong, C. Chen, Q. Peng, D. Wang, Y. Li, *Hollow N-Doped Carbon Spheres with Isolated Cobalt Single Atomic Sites: Superior Electrocatalysts for Oxygen Reduction*, Journal of the American Chemical Society, 139, 17269–17272, 2017.
20. E. J. Biddinger, D. Von Deak, D. Singh, H. Marsh, B. Tan, D. S. Knapke, U. S. Ozkan, *Examination of Catalyst Loading Effects on the Selectivity of CN<sub>x</sub> and Pt/VC ORR Catalysts Using RRDE*, Journal of the Electrochemical Society, 158, B402-B409, 2011.
21. A. Bonakdarpour, M. Lefevre, R. Yang, F. Jaouen, T. Dahn, J. -P. Dodelet, J. R. Dahn, *Impact of Loading in RRDE Experiments on Fe–N–C Catalysts: Two- or Four-Electron Oxygen Reduction?*, Electrochemical and Solid-State Letters, 11, B105-B108, 2008.

22. D. Y. Chung, M. J. Kim, N. Kang, J. M. Yoo, H. Shin, O. -H. Kim, Y. -E. Sung, *Low-Temperature and Gram-Scale Synthesis of Two-Dimensional Fe–N–C Carbon Sheets for Robust Electrochemical Oxygen Reduction Reaction*, Chemistry of Materials, 29, 2890-2898, 2017.
23. Y. Mun, M. J. Kim, S. A. Park, E. Lee, Y. Ye, S. Lee, Y. -T. Kim, S. Kim, O. -H. Kim, Y. -H. Cho, Y. -E. Sung, J. Lee, *Soft-template synthesis of mesoporous non-precious metal catalyst with Fe-N<sub>x</sub>/C active sites for oxygen reduction reaction in fuel cells*, Applied Catalysis B: Environmental, 222, 191-199, 2018.
24. J. Sanetuntikul, C. Chuaicham, Y. W. Choi, S. Shanmugam, *Investigation of hollow nitrogen-doped carbon spheres as non-precious Fe–N<sub>4</sub> based oxygen reduction catalysts*, Journal of Material Chemistry A, 3, 15473-15481, 2015.
25. C. Chen, X.-D. Yang, Z.-Y. Zhou, Y.-J. Lai, M. Rauf, Y. Wang, J. Pan, L. Zhuang, Q. Wang, Y.-C. Wang, N. Tian, X. -S. Zhang, S. -G Sun, *Aminothiazole-Derived N, S, Fe-Doped Graphene Nanosheets as High Performance Electrocatalysts for Oxygen Reduction*, Chemical Communications, 51, 17092-17095, 2015.
26. Y. J. Sa, C. Park, H. Y. Jeong, S. H. Park, Z. Lee, K. T. Kim, G -G Park, S. H. Sang, *Carbon Nanotubes/Heteroatom-Doped Carbon Core–Sheath Nanostructures as Highly Active, Metal-Free Oxygen Reduction Electrocatalysts for Alkaline Fuel Cells*, Angewandte Chemie International Edition, 126, 4186-

4190, 2014.

27. L Zhang, DP Wilkinson, Y Liu, J Zhang, *Progress in nanostructured (Fe or Co)/N/C non-noble metal electrocatalysts for fuel cell oxygen reduction reaction*, *Electrochimica Acta*, In press, 2018.

## 초록

# 백금 및 비귀금속 촉매를 이용한 음이온 교환막 연료전지의 성능에 미치는 전극 인자들

양이온 교환막 연료전지는 운전 중 온실가스가 발생하지 않는 전기 화학적 에너지 변환 장치로, 기존의 화석 연료를 대체할 에너지원으로써 집중적인 연구가 진행되어왔다. 그러나 고가의 귀금속 촉매 사용으로 인한 낮은 가격 경쟁성과 단가 절감의 한계로 인해 연료 전지의 시장 확대에 어려움을 겪고 있다. 이에 음이온 교환막의 개발과 더불어, 양이온 교환막 연료전지를 대체할 유망한 연료전지로 음이온 교환막 연료전지가 주목받고 있다. 기존의 양이온 교환막 연료전지보다 음이온 교환막 연료전지가 갖는 장점은 탄화수소 연료 산화에 대한 낮은 과전압으로 인한 우수한 연료 유연성, 음극 연료의 반대 방향으로의 교차가 억제됨에 따른 높은 연료 효율성 그리고 금속 물질의 부식 현상 감소가 있다. 특히, 알칼리 분위기에서의 산소 환원 과전압이 산 분위기에 비교해 현저히 감소함에 따라 저가의 비귀금속 계의 산소 환원 촉매의 사용은 가장 큰 이점으로

여겨진다. 이에 따라 백금과 상응할 만한 우수한 산소 환원 활성을 나타낼 수 있는 비귀금속 촉매의 개발 연구가 활발히 진행되었다. 그러나 현재 백금보다 우수한 성능을 나타낸다고 보고한 비귀금속 촉매는, 실질적인 연료 전지 구동 환경인 단위 전지 성능에서 백금보다 우수한 성능을 반영하지 못하고, 반쪽 전지만의 성능 구현에 그쳤다는 한계를 보인다. 이는 촉매를 반쪽 전지가 아닌 단위 전지에 적용하였을 경우 우수한 성능 구현을 위한 중요 전극 인자가 달라지기 때문이다. 반쪽 전지에서의 성능에 영향을 미치는 인자에 대한 연구는 활발히 진행되었으나, 촉매를 단위 전지에 적용했을 때 중요한 인자들에 대한 연구는 부족한 실정이다. 이러한 인자의 차이가 나타나게 되는 이유 중 하나는 성능 측정 시의 다른 전해질 유형을 사용하기 때문이다. 반쪽 전지의 경우 액체 전해질을 사용하기 때문에 촉매의 거의 모든 활성점이 반응에 참여하지만, 단위 전지의 경우 고체 전해질을 사용하기 때문에 이와 맞닿아있는 활성점만이 실제 성능에 기여하게 된다. 따라서 고체 전해질의 특성 및 촉매 층 내에서의 고체 전해질의 분포 상태는 전극 층의 이온 전도도 및 미세 구조를 결정하므로 단위 전지의 성능에 상당한 영향을 미친다. 또 다른 이유는 반응물과 생성물의 공급이 반쪽 전지에 비교해 훨씬 복잡하기 때문이다. 음이온 교환막 연료전지의 경우, 물은 수소 산화 반응의 결과로 음극에서 생

성물이면서 양극에서는 산소 환원 반응에 참여하는 반응물이다. 이에 따라 단위 전지 내에서의 물 관리는 훨씬 더 복잡해지며 이온 및 농도 과전 압 측면에서 매우 중요하다. 따라서, 본 학위 논문에서는 백금과 비귀금 속 촉매를 음이온 교환막 연료전지에 적용하여 단위 전지 구동 조건에서의 성능에 중요한 전극 인자들에 대해 논하고자 한다.

1장에서는 연료 전지의 전반적인 개요 및 음이온 교환막 연료전지의 작동 원리와 주요 현안에 대해 언급하였다.

2장에서는 백금 촉매를 기반으로 하는 음이온 교환막 연료전지에서 성능에 중요한 전극 인자들을 조사하였다. 먼저 막-전극 접합체를 음이온 교환막 연료전지에 도입하기 전 간단한 처리를 거침으로써 전극 내 수산화 이온의 전도를 최적화하였다. 막-전극 접합체의 개선된 저항 특성은 분극 곡선 및 임피던스 분광 분석 결과를 통해 확인할 수 있었다. 특히 높은 촉매 사용량이 요구되는 비귀금속 촉매를 적용했을 경우 백금 촉매보다 더 큰 성능 개선 폭을 보였다. 다음으로 촉매 잉크의 용매의 유전성을 조절하여 전극 내 이차 기공 구조를 발달시킴으로써 성능이 향상될 수 있음을 확인하였다. 끓는 점이 유사한 용매 중 유전 상수의 차이가 있는 t-뷰탄올, 에탄올, 2-프로판올을 사용하였을 때 용매의 종류에 따라 촉매 입자 간의 기공 구조인 이차 기공 구조의 차이가 나타났다. 이차 기

공 구조가 발달함에 따라 더 우수한 물질 확산 및 이온 전도 특성을 나타내었다. 마지막으로 음극과 양극에 사용되는 기체 확산층의 특성이 성능에 미치는 영향을 확인하였다. 음극에 소수성의 기체 확산층이 도입되었을 때 음극에서 생성된 물의 역 확산이 촉진되어 한계 전류 밀도가 증가하는 것을 확인하였다.

3장에서는 비귀금속 촉매 중에서 가장 성능이 우수한 촉매로 보고 된 철-질소-탄소 복합체의 촉매를 양극 산화 환원 촉매로 적용한 음이온 교환막 연료전지에 대해 연구하였다. 앞선 백금 기반의 실험을 통해 밝혀진 성능에 중요한 인자를 고려한 비귀금속 촉매의 구조를 설계하였다. 현재 우수한 산소 환원 활성을 나타낸다고 보고한 비귀금속 촉매는 반쪽 전지만의 성능을 기반으로 하며, 특히 이때 비귀금속 촉매의 사용량은 백금 촉매 대비 최소 5배 이상을 사용한다. 이에 실제 구동 환경인 단위 전지에서 같은 비율로 적용할 시 비귀금속 촉매의 경우 두꺼운 전극 층으로 인해, 반쪽 전지의 경우와는 달리, 물질 전달 및 오믹 저항이 증가하며 단위 전지의 성능을 감소시키는 주된 요인으로 작용한다. 이에 두 가지 방식으로 비귀금속 촉매의 성능을 개선하고자 하였다. 반응 물질의 확경로를 감소시킬 수 있는 2차원의 탄소 시트를 적용하였고, 일반적인 탄소 지지체인 탄소 블랙과 비교했을 때 더 높은 성능을 나타내는 것을 확

인하였다. 다음으로 마크로 기공 구조를 촉매 층에 도입하여 물질 전달 및 오믹 저항을 감소시키고자 하였다. 그 결과 마크로 기공 구조가 상대적으로 덜 빌달한 촉매에 비교해 향상된 성능을 보이며, 다른 조건이 같은 경우 백금 촉매가 적용된 음이온 교환막 연료전지와 상응할 만한 개선된 성능을 나타냈다.

**주요어:** 막-전극 접합체, 음이온 교환막 연료전지, 전극 구조, 비귀금속 촉매, 전기화학

**학 번:** 2013-30278